Determining the number of fibre-fibre contacts in cardboard samples using tomographic imaging.

M.Sc. Thesis

Axel Artur Ekman

UNIVERSITY OF JYVÄSKYLÄ

Jyväskylä university
Department of Physics
Spring 2011

ABSTRACT

The fibrous network of cardboard samples was studied with the aid of tomographic imaging. For analysing the samples a method of determing the number of contacts between fibres in a planar fibrous network was introduced. The model is based on the fact that deposited paper-like structures tend to have predominantly planar fibre orientation. With this assumption an expression of the mean segment length was derived in terms of the average shortest path along fibres through the sample in the out-of-plane direction.

The density profiles of cardboard samples were analysed by determing four quantitative features, the solids content, standard deviation of the solids content, slope and curvature. All the samples had a slope in the same direction, i.e., they were denser at the bottom surfaces. Densification seems to occur at both surfaces, as the curvature was larger for samples with higher solids content.

Our measurements indicate that contact densities of the cardboards, i.e., the number of fibre-fibre contacts per unit volume are proportional to the square of the solids content. This is in agreement with earlier models for three-dimensional fibre networks.

PREFACE

The work reported in this Thesis was carried out between autumn 2009 and spring 2011 at the Department of Physics, University of Jyväskylä. First and foremost I want to express my gratitude to Stora Enso for providing me with both an iteresting problem and the samples on which the research is based.

I am also grateful for the encouragement and assistance recieved from my supervisor Jussi Timonen throughout the process. I am also pleased to acknowledge Arttu Miettinen and Tuomas Turpeinen for their assistance regarding image analysis.

Axel Ekman
March 2011
Jyväskylä

CONTENTS

1. INTRODUCTION

The initial motivation for this Master's Thesis was to investigate how tomography could aid studies of paper-like materials. Tomography is a reasonably new tool for studying fibres and fibre networks, probably owing to the recent improvement in tomographic imaging and the capability to image paper-like materials with sufficient spatial resolution.

The research was focussed on a set of 8 cardboard samples. Although it is widely known that the out-of-plane strength usually correlates quite well with cardboard density [12, 14], there were samples that deviated quite noticeably from this trend. The main purpose of this work was to get insight into these cases. The out-of-plane strength of cardboard is an important property in many cases of end use. Delamination can occur, for example, at glue seams in packaging and in the coating process. Stresses can also otherwise be subjected to cardboard in the out-of-plane direction. It is also in the best interests of both the consumer and the manufacturer to reduce production costs by using minimal amounts of raw materials while maintaining the desired strength properties.

The process of forming paper-like materials starts with a suspension of water, fibres and possible additives and fines. The initial solids content of the suspension is less than one percent. In this concentration the solids move around quite freely in the suspension. After the initial drainage of water, the solid content increases to about 20 percent [14]. After drainage, the fibres are more or less in place and cannot move freely. Thereafter further water removal takes place by wet pressing and drying. The stochastic nature of the forming of paper lies in the initial drainage. After the initial drainage, fibrous networks formed this way have predominantly planar

orientation. This layered planar structure of the final product has led to the primary description of the paper structure as a two-dimensional network [3].

Based on the assumption that cardboard consists of stiff fibres that all have a planar orientation, we derived an equation for the total number of contacts in a sample. The fibre network model used here is strongly based on random fibre networks that follow a Poisson process [3]. The average segment length between two adjacent fibre-fibre contacts was determined by applying a distance transform on a tomographic image of the sample, from which we determined the shortest paths between two parallel planes along the fibres in the sample. From this data, the average segment length of the network was derived assuming that sections of the path, which are in the thickness direction of the sample, only appear at fibre-fibre contacts. Four sets of samples were imaged with high resolution micro-computed tomography (micro-CT) using two different magnifications.

A method for binarizing the tomographic images was developed based on measured values for the area density of the samples, which was concluded to be the most reliable measurement on the cardboards. By assigning the solid content of the image with a fixed density, the area density of the samples could be expressed as a function of the threshold gray value. The same tomographic images were also used to determine the density profiles of the samples. From these density profiles four quantitative values were determined. These were the mean solids content, standard deviation, slope and curvature.

Our measurements indicate that the contact density, i.e., the number of contacts per unit of volume, is proportional to the square of the solids content of the network. Earlier theoretical models for random fibrous materials support this result.

It seems that the relation between solids content and contact density is governed by fibre properties alone. Different additives may increase the number of contacts formed in the papermaking process, but not without increasing at the same time the density. From the density profiles we could

conclude that the bottom surfaces of the samples were always denser than the average density. Moreover, densification seems to occur at both surfaces.

The basics of tomography is covered in chapter 2. This includes the basic principles of tomography and a quality-based reasoning for the used parameters in the measurements. In chapter 3 the properties of a two-dimensional stochastic network is explained, and the theory is expanded to include three-dimensional networks. The model for determining the contact density from a tomographic image is introduced in chapter 4, and the required image analysis is described in chapter 5. The measurements preformed and their results are reported in chapter 6. Final conclusions and an evaluation of the new method for determining the density of fibre-fibre contacts are given in chapter 7.

2. X-RAY COMPUTED TOMOGRAPHY

X-ray computed tomography (x-ray CT) is an imaging method, where the structure of the sample is derived from x-ray radiographs taken from many different angles. Although the mathematics required was established as early as 1917 by Radon, the first practical use of the method was introduced much later. The first commercial device was developed by Hounsfield in the early 1970's and tomography soon became a frequently used imaging method in medical science. Only recently has the resolution of CT scanners become good enough to be suitable for imaging paper and cardboard. Scanners with a resolution in a μm scale are called micro-CTs or μCT. This chapter is intended to clarify the function of μCT devices and to give reason for the imaging parameters used.

2.1 X-ray imaging

Generally desktop μCT devices consist of an x-ray source, a rotating sample holder and a detector fig. (2.1). By rotating the sample holder, radiographs of the object can be taken from different angles. From these radiographs, a reconstruction of the object is made.

2.1.1 Generation of X-rays

In all desktop CT scanners, the beam is produced with an x-ray tube. In the simplest form, an x-ray tube consists of a cathode filament which emits electrons that are collected at an anode plate, fig. (2.2). When electrons strike the anode plate they deaccelerate, producing Bremsstrahlung and

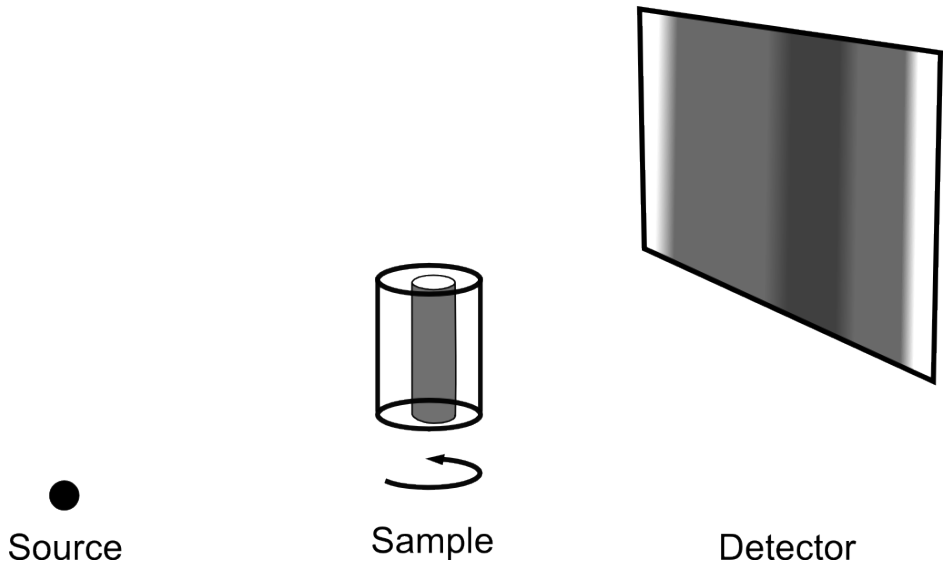

Fig. 2.1: The basic function of a CT device. Radiographs are taken of the sample from different angles. The three dimensional structure of the sample is reconstructed from these radiographs.

characteristic radiation depending on the anode material. The x-ray tube emits photons in all directions, so a pinhole or collimator is needed to narrow the beam. This means that most of the emitted x-rays never encounter the imaged sample.

2.1.2 Interaction with matter

X-ray imaging is based on x-ray attenuation. When monochromatic x-rays pass trough a homogeneous object, the intensity of the beam follows the Beer-Lambert law

$$I = I_0 e^{-\mu x}, \tag{2.1}$$

where I_0 is the unattenuated beam, x the thickness of the object and μ the linear attenuation coefficient. Rewriting eqn (2.1) in terms of the mass attenuation coefficient μ/ρ

$$I = I_0 e^{-\frac{\mu}{\rho}\rho x}. \tag{2.2}$$

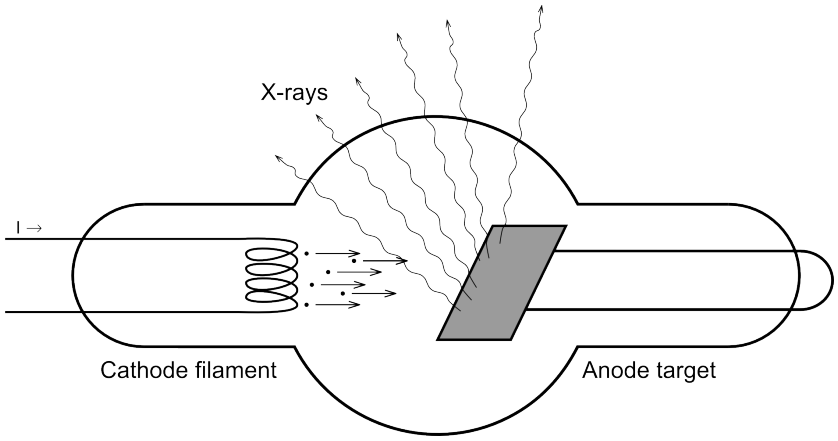

Fig. 2.2: Emitted electrons from the filament are accelerated towards the target anode. When they strike the target, they interact with the material and deaccelerate, producing a spectrum of x-rays that consists of Bremsstrahlung and characteristic peaks depending on the material of the anode.

The mass attenuation coefficient is a material property that depends strongly on the atomic number Z and the wavelength of the x-ray, λ.

The attenuation of x-rays interacting with the specimen is primarily governed by three effects: photoelectric absorption, coherent scattering and Compton scattering. The probability of such events happening all depend strongly on the atomic number of the material and the energy of the x-ray. Thus, for a polychromatic beam, attenuation has to be integrated over the energy spectrum,

$$I = \int I_0(E)\, e^{-\frac{\mu(E)}{\rho}\rho x}\, \mathrm{d}E. \tag{2.3}$$

However, calculating such integral is usually quite problematic. For practical purposes, an effective mass attenuation coefficient is used. This may lead to some artefacts in the reconstruction such as beam hardening (low-energy x-rays are more likely to be absorbed and cause the energy spectrum to 'harden' as the beam passes through the specimen). The use of an effective mass attenuation coefficient also gives reason for why it is important to image samples with the same parameters if any comparison is going to be made.

2.1.3 Imaging and reconstruction

For the sake of simplicity, let us assume a parallel monochromatic beam passing through a sample. We can rewrite eqn (2.2) in a differential form, i.e., the attenuation that occurs within a small thickness element ds is given by

$$\frac{\mathrm{d}I}{I} = -\frac{\mu}{\rho}\rho\,\mathrm{d}s = -f(x,y)\,\mathrm{d}s. \tag{2.4}$$

Now for any slice, a row in the radiograph represents a projection function, i.e., an integral over lines trough the sample

$$P(t) = \int_{line(t)} f(x,y)\,\mathrm{d}s. \tag{2.5}$$

Now consider a coordinate system that is a rotated with respect to the (x,y) one,

$$\begin{bmatrix} t \\ s \end{bmatrix} = \begin{bmatrix} \cos\theta & \sin\theta \\ -\sin\theta & \cos\theta \end{bmatrix} \begin{bmatrix} x \\ y \end{bmatrix}. \tag{2.6}$$

For a rotation by angle θ the projection function now becomes

$$P_\theta(t) = \int_{-\infty}^{\infty} f(t,s)\,\mathrm{d}s. \tag{2.7}$$

The Fourier transform of the projection data for one slice at angle θ can be written as

$$S_\theta(\omega) = \int_{-\infty}^{\infty} P_\theta(t) e^{-i2\pi\omega t}\,\mathrm{d}t. \tag{2.8}$$

Substituting $P_\theta(t)$ of eqn (2.7) and transforming into the (x,y) coordinate system by the relation eqn (2.6) we find that

$$S_\theta(\omega) = \int_{-\infty}^{\infty}\int_{-\infty}^{\infty} f(x,y) e^{-i2\pi\omega(x\cos\theta + y\sin\theta)}\,\mathrm{d}x\mathrm{d}y, \tag{2.9}$$

which is conveniently just the two dimensional Fourier transform of a function $f(x,y)$

$$F(u,y) = \int_{-\infty}^{\infty}\int_{-\infty}^{\infty} f(x,y) e^{-i2\pi(ux+vy)}\,\mathrm{d}x\,\mathrm{d}y, \tag{2.10}$$

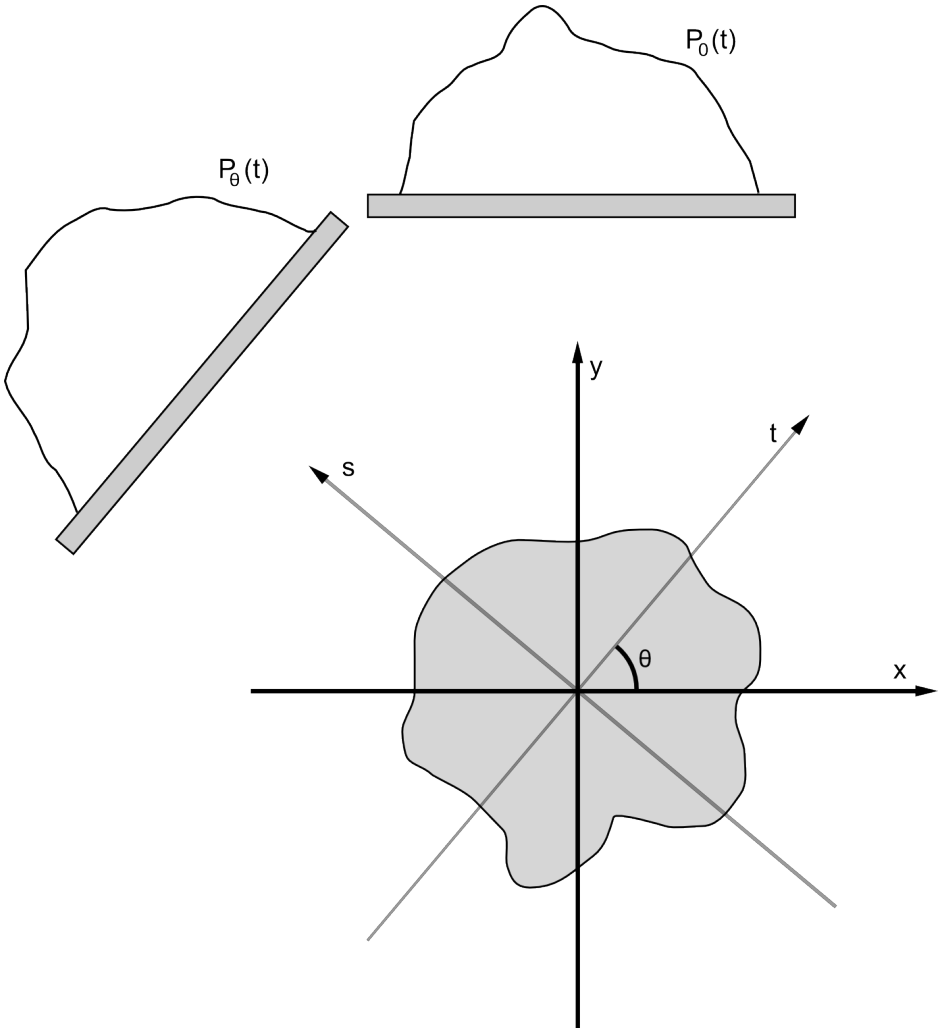

Fig. 2.3: Sample and its two projections, one at angle 0, $P_0(t)$, and another at angle θ, $P_\theta(t)$.

with the constraints $u = \omega \cos\theta$ and $v = \omega \sin\theta$, which in this case describe the line of the projection. So for every Fourier transform of projection $P_\theta(t)$ we fill the frequency domain at angle θ. Consequently, collecting an infinite number of projection data at different angles would result in a complete Fourier transform of the object.

2.1.4 Filtered backprojection

The most commonly used reconstruction method for tomographic images is filtered backprojection or some algorithm based on it. Although most desktop micro-CTs use cone beam geometry, the mathematics involved is excluded here. In a fan beam geometry one may simply rearrange the beams so as to get an approximation of a parallel beam geometry [9, 17]. Cone beam reconstruction is based on the approximation that by applying some corrections to the projected data based on the beam geometry, filtered backprojection can be used to acquire the reconstructed image [4, 9].

The inverse Fourier transform of $F(u, v)$ is given

$$f(x, y) = \int_{-\infty}^{\infty} \int_{-\infty}^{\infty} F(u, v) e^{i2\pi(ux+vy)} \, \mathrm{d}u \, \mathrm{d}v. \tag{2.11}$$

Expressing this in polar coordinates by making the substitution $u = \omega \cos\theta$ and $v = \omega \sin\theta$, eqn (2.11), and by substituting the Fourier transform of the projection at angle θ, $S_\theta(\omega)$, for the Fourier transform $F(\omega, \theta)$, one can express the transform in the form

$$f(x, y) = \int_0^{\pi} \int_0^{\infty} S_\theta(\omega) |\omega| e^{i2\pi\omega t} \, \mathrm{d}\omega \, \mathrm{d}\theta. \tag{2.12}$$

By substituting eqn (2.8) for $S_\theta(\omega)$ and rearranging, we find that

$$f(x, y) = \int_0^{\pi} \int_0^{\infty} P_\theta(t') G_\theta(t - t') \, \mathrm{d}t' \, \mathrm{d}\theta, \tag{2.13}$$

where $G_\theta(t - t') = \int |\omega| e^{i2\pi\omega(t-t')} \, \mathrm{d}\omega$. This is the underlying idea of the filtered backprojection. A filter, G_θ, is applied to the projections P_θ. The result is 'smeared' or backprojected onto the image as in fig(2.4) . The reconstructed image consists of contributions of this backprojection from each angle θ.

2.2 Xradia Micro-XCT-400

The micro-CT device for the measurements was the Xradia Micro-XCT-400. The device is a quite flexible micro-CT system with a large range of

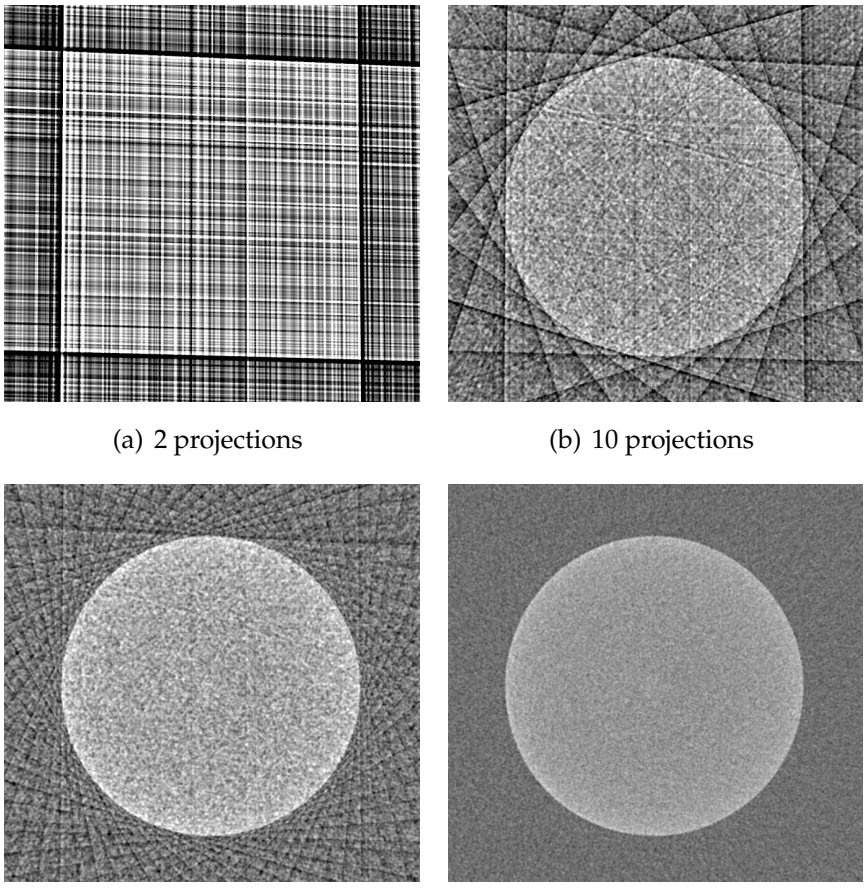

(a) 2 projections (b) 10 projections

(c) 30 projections (d) 181 projections

Fig. 2.4: A slice of a ruby ball, reconstructed by using a varying number of projections.

capabilities. The device uses an standard x-ray tube with an acceleration voltage up to 90 kV. It is equipped with four magnification objectives: 0.5x, 4x, 10x and 20x. The flexibility of the system enables studies of how different parameters affect the resulting image quality as well as optimization of parameters for a specific material.

2.3 Image quality and parameters

For a system as flexible as the one used, it is important to know what parameters affect the quality of the resulting image. In medical science one has to take into account that the dosage received by the patient must be kept low. For use in material science this is not the case. Three parameters were optimized: acceleration voltage, exposure time and the number of projections. The recommended settings for the geometrical parameters, i.e., source and detector distance were assumed optimal. The image quality tests were done with a magnification of 10x. For the tomographic images using the 4x objective, the same acceleration voltage was used. The exposure time was adjusted so as to maximize the image quality while not overexposing the CCD-chip, and the number of projections was chosen based on the experimental results from the 10x measurements.

The imaging parameters used for the chosen samples were determined experimentally by taking images with different settings. The measure of quality used was the contrast to noise ratio defined as

$$CNR \equiv \frac{S_A - S_0}{\sigma_0}, \tag{2.14}$$

where S_A and S_0 are the gray scale values of the signal and void, respectively, and σ_0 is the standard deviation of the void.

2.3.1 Tube voltage

A series of x-ray radiographs of a cardboard was taken with the different acceleration voltage, varying from 20 kV to 90 kV with a constant power of 4 W. No measurements were done with a voltages below 20 kV because of the limitation in the maximum current. The sample was placed so that a half of the field of view was screened by it. All radiographs were taken without moving the sample between imaging. The values for determining the CNR were measured from the same section (region of interest, ROI) of the images.

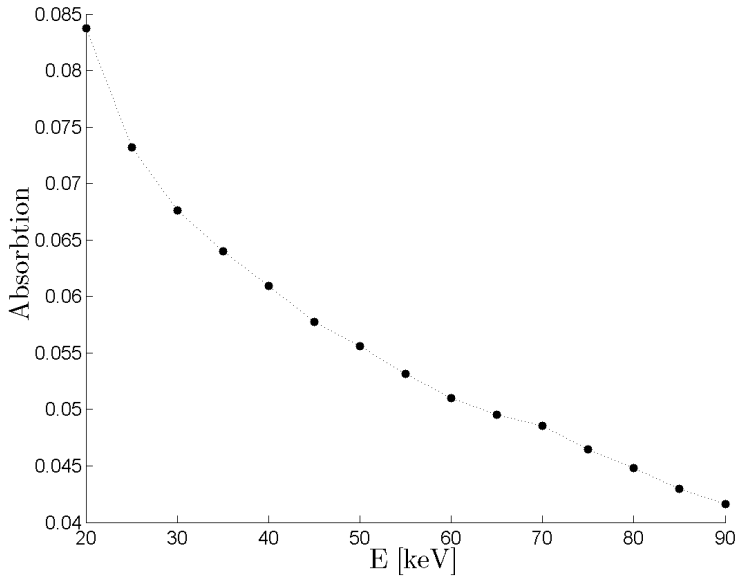

Fig. 2.5: Absorption coefficient of the seclected ROI as a function of tube voltage. The higher the accelration voltage, the higher the probability for photon transmission through the sample, which results in a smaller absorption coefficient.

2.3.2 Exposure time

Measurements were done in the same way as for the tube voltage, but by varying the exposure time in the range of 30 seconds to 10 minutes, i.e., from 6% to 80% of the capability of the CCD.

The probability of a photon to be detected is governed by two probabilities. The number of photons at energy $\bar{e}$ emitted by the x-ray source follows a Poisson distribution [8] with some mean value λ. The probability that an emitted photon reaches and is counted by the detector is $\rho\sigma$, where ρ is the transmittance and σ is the detector efficiency. Combining these probabilities, Poisson and binomial, it can be shown that the probability $P(x)$ that in one unit time exactly x photons are counted by the detector is given by

$$P(x) = \frac{(\lambda\rho\sigma)^x}{x!} e^{-\lambda\rho\sigma}, \tag{2.15}$$

i.e., a Poisson distribution with the mean $\lambda\rho\sigma$ and a standard deviation of $\sqrt{\lambda\rho\sigma}$. This means that our measure of quality, eqn (2.14), behaves as $CNR \propto \sqrt{\lambda\rho\sigma}$. The result of this measurement is shown in fig. (2.6).

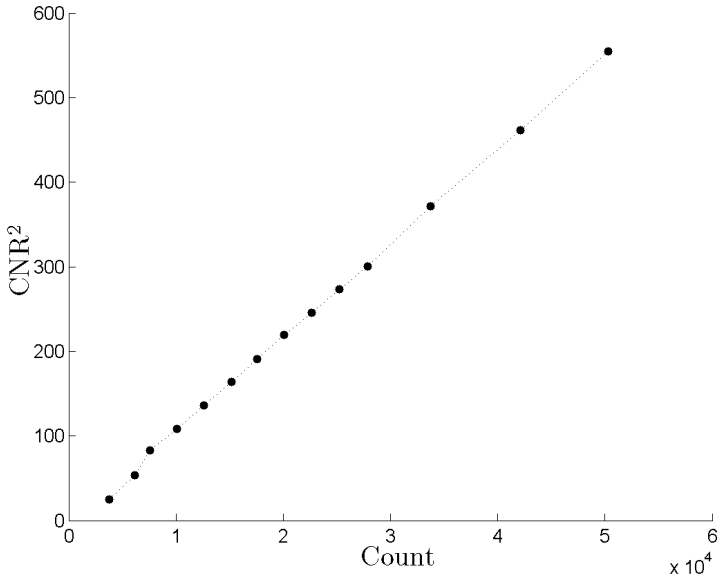

Fig. 2.6: CNR^2 as a function of exposure time (counts). The results of the measurements show that the square of the CNR is linearly dependent on the number of counts. The error in the lower counts is likely to be caused by inproper warmup of the source.

2.3.3 Number of projections

The effect of the number of projections was examined by taking a reference image with 1850 projections. The radiographs were exported and new data sets were made by using a fraction of the original radiographs. All the tomographic images were reconstructed with the same parameters. A ROI was made for measuring the signal by combining thresholded images of the different reconstructions. The threshold gray value was chosen large enough to be sure that the remaining voxels represent the signal. The void was measured by defining 5 areas of empty space within the sample, and using the same ROI for every image.

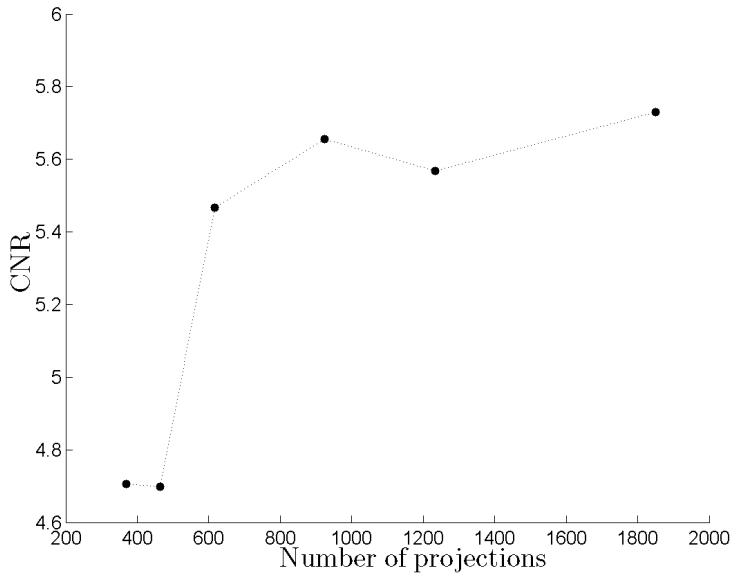

Fig. 2.7: CNR as a function of the number of projections. The measurements demostrate that after a sufficient number of projections the quality of the reconstructed image does not seem to improve notably.

2.3.4 Chosen parameters for imaging cardboard

According to the manufacturer, the optimum operating power for the x-ray tube is 4 W. As seen in fig. (2.5) the absorption coefficient of the cardboard sample increases with decreasing acceleration voltage, therefore an acceleration voltage of 20 V was used. The exposure time and number of projections was chosen based on three factors, viz., the manufacturer recommends not to use more than 50 % of the capability of the CCD-chip, the quality does not seem to improve notably by increasing the number of projections beyond 900, and for practical reasons the total scanning time was desired to be less than 24h. The exposure time was chosen to be 90 s and 4 projections were taken per degree of rotation resulting in a total of 745 projections.

3. STOCHASTIC FIBRE NETWORKS

The actual forming of a paper like fibrous material from an aqueous suspension to a final product is really a three dimensional process. However, analyzing the final product one may easily notice that most papers have a strongly two dimensional, layered structure [3]. Owing to this, the standard way to approach the structure of paper like materials is by considering it a stack of two dimensional random fibre networks [11]. The statistical geometry of a strictly two dimensional network is quite well understood. Corte and Kallmes defined such a network to be one where less than 1% is covered by more than two fibres [10]. In this chapter, the geometry of two dimensional stochastic fibre networks is described and some generalizations for three dimensional networks are introduced.

3.1 Two dimensional random fibre networks

3.1.1 Coverage

The standard model for describing a two dimensional random network of fibres is by assuming that the fibre centres are positioned according to a Poisson process and the fibre orientation has a uniform distribution [3]. To explain this let us consider an area A, where N_f fibres are dropped such that the distribution of the centres of mass of the fibres and of their orientation are uniform. Now, for any point in area A, the probability that exactly n fibres cover that point follows the binomial distribution,

$$P_{\mathrm{c}}(n) = \binom{N_{\mathrm{f}}}{n} (p)^n (1-p)^{N_{\mathrm{f}}-n}, \tag{3.1}$$

where p is the probability for a single fibre to cover the chosen point. If N_f is large, p is small and $N_f p$ is of moderate magnitude, the distribution reduces to the Poisson approximation of the binomial distribution,

$$P_c(n) \approx \frac{(N_f p)^n e^{-N_f p}}{n!}. \tag{3.2}$$

The quantity $N_f p$ is called the coverage of the fibre network, i.e., the average number of fibres covering a point. For a random network of this type with mean coverage of $\bar{c}$, the probability of finding coverage $c = n$ is [3] given by

$$P_c(n) = \frac{\bar{c}^n}{n!} e^{-\bar{c}}. \tag{3.3}$$

The mean coverage can be expressed in form of the grammage, i.e. the area density of the network, and fibre coarseness, i.e. the weigth per fibre length, or in terms of the projected fibre area,

$$\bar{c} = \frac{\beta w_f}{\delta} = \frac{N_f w_f l_f}{A}, \tag{3.4}$$

where β is the grammage, w_f the fibre width, δ the fibre coarseness and f the fibre length.

3.1.2 Number of crossings per fibre

For a two dimensional randomly deposited network of long straight fibres with an uniform distribution of orientation, Corte and Kallmes [10] derived the total number of crossings in an area A containing N_f fibres (n_c).

For any given fibre, the probability that a deposited fibre intersects it is given by

$$P_{int} = \frac{l_f^2}{\pi A} \int_0^{\pi} |sin\theta| \, d\theta = \frac{2 l_f^2}{\pi A}. \tag{3.5}$$

Considering that the fibre cannot intersect itself, the number of events is then $^1/_2 N_f(N_f - 1)$. If the number of fibres is large, $N_f >> 1$, the number of intersections is

$$n_c = P_{int} \frac{N_f(N_f - 1)}{2} = \frac{(N_f l_f)^2}{\pi A}. \tag{3.6}$$

Assuming that an intersection is always between two fibres, we find for the number of crossings per fibre (n_{cf}) the result

$$n_{\mathrm{cf}} = \frac{2N_{\mathrm{f}}l_{\mathrm{f}}^2}{\pi A}. \tag{3.7}$$

3.1.3 Segment length

Now consider a Poisson process along a fibre. For a fixed interval at length x, and the mean number of crossings per unit length μ, the probability of finding k crossings in the interval is [3] given by

$$P(k) = \frac{(\mu x)^k}{k!}e^{-\mu x},\ k = 0, 1, 2, \ldots . \tag{3.8}$$

The probability of finding zero crossings in the interval is then

$$P(0) = e^{-\mu x},\ x > 0. \tag{3.9}$$

Normalizing, we find that the probability of finding a gap of length x along a fibre with a mean gap length of μ^{-1} is given by

$$P_{\mathrm{length}}(x) = \mu e^{-\mu x},\ x > 0. \tag{3.10}$$

If a fibre has a total of n_{cf} intersections with other fibres, it is divided into $n_{\mathrm{cf}} + 1$ segments. Using eqn (3.7), we find that the average segment length l_{seg} is given by

$$l_{\mathrm{seg}} = \frac{l_{\mathrm{f}}}{n_{\mathrm{cf}} + 1} = \frac{l_{\mathrm{f}}}{\frac{2(N_{\mathrm{f}}l_{\mathrm{f}})^2}{\pi A N_{\mathrm{f}}} + 1}. \tag{3.11}$$

If $N_{\mathrm{f}}l_{\mathrm{f}}^2 >> A$, i.e., the network is dense enough this can be expressed in the form

$$l_{\mathrm{seg}} = \frac{\pi A}{2N_{\mathrm{f}}l_{\mathrm{f}}}. \tag{3.12}$$

3.2 Three dimensional random fibre networks

In a three dimensional network, all the crossings that appear in the projection of the network to the xy-plane are not connected, as distances in the third dimension between the fibres disappear. In eqn (3.6) the total number of contacts was determined by counting all the intersections between the fibres. If a network has local coverage 3 or greater, the assumption overestimates the number of contacts. As an upper bound, we consider the case where the fibres are flexible enough so that every possible contact is made.

For every crossing with a coverage of two, the fibres have a total of one intersection and there is one contact. For a crossing with coverage of three, the fibres would have a total of three intersections and two contacts. Correspondingly for a crossing with coverage of n, there is a total $\binom{n}{2}$ intersections and $n-1$ contacts. We thus find that the number of contacts for flexible fibres is given by

$$n_b = a_{\text{flex}} n_{\text{c}} \qquad a_{\text{flex}} = \sum_2^\infty \frac{P_c(x)}{1 - P_c(0) - P_c(1)} \frac{x-1}{\binom{x}{2}}, \tag{3.13}$$

which can be written in the form (appendix (A.1))

$$n_b = a_{\text{flex}} n_{\text{c}} \qquad a_{\text{flex}} = \frac{2}{e^{\bar{c}} - \bar{c} - 1} \left[\text{Ei}(\bar{c}) - ln(\bar{c}) - \bar{c} - \gamma \right], \tag{3.14}$$

where $\text{Ei}(x)$ is the exponential integral and γ is the Euler-Mascheroni constant. This upper limit for the fraction of intersections that are in contact is shown in fig. (3.1). As expected, the larger the coverage the more the network deviates from the two dimensional approximation (mean coverage ~ 0.5).

For stiffer fibres, only a fraction of the crossings are in contact. We denote the fraction of actual contacts among the crossings in the projection by a constant a as in ref. [20]. In this way we find for the number of contacts in three dimensions the result

$$n_{\text{b}} = a n_{\text{c}} \qquad a \leq a\text{flex}. \tag{3.15}$$

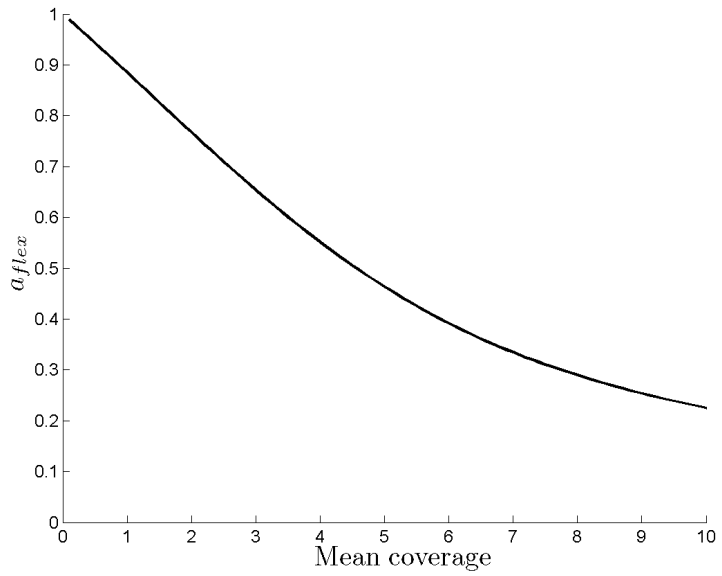

Fig. 3.1: a_{flex} as a function of mean coverage.

As explained in [13], for fibre networks of low coverage, the constant a only affects the frequency of the Poisson distribution. As the thickness of the network increases, it is no longer reasonable that the contacts are uncorrelated. This will certainly contribute to some error in determining the mean segment length, but owing to the lack of any other reasoned length distribution, we will use the one described in eqn (3.10). Using the same assumptions as in eqn (3.12), we can derive the average segment length for a three dimensional network such that

$$l_{\text{b}} = \frac{1}{a}\frac{\pi A}{2N_{\text{f}}l_{\text{f}}}. \tag{3.16}$$

4. SHORTEST PATH ANALYSIS

In this chapter expressions for the average segment length and number of contacts for a network of stiff planar fibres are derived by considering the shortest path along fibres between two parallel planes in a three dimensional network.

4.1 Three dimensional fibre network

The total mass of a sample of cardboard is the sum of the masses of all fibres (assuming that there are no other solid components). On the other hand, we can calculate the mass of the cardboard via its density. In this way we find that

$$N_{\mathrm{f}} m_{\mathrm{f}} = V \phi_{\mathrm{s}} \rho_{\mathrm{f}}, \tag{4.1}$$

where N_{f} is the number of fibres, m_{f} the average mass of a fibre, V a control volume, ϕ_{s} the fraction of solids contents and ρ_{f} the density of the cell-wall. The average number of fibres in a control volume is now given by

$$N_{\mathrm{f}} = \frac{V \phi_{\mathrm{s}} \rho_{\mathrm{f}}}{m_{\mathrm{f}}} = \frac{V \phi_{\mathrm{s}}}{A_{\mathrm{f}} l_{\mathrm{f}}}, \tag{4.2}$$

where A_{f} is the average cross-sectional area of the fibres and l_{f} the average fibre length. As in eqn (3.11), the number of contacts (n_{bf}) on a fibre can be approximated such that

$$n_{\mathrm{bf}} = \frac{l_{\mathrm{f}}}{l_{\mathrm{b}}} - 1, \tag{4.3}$$

where l is average segment length, i.e., the average distance between adjacent contacts. Supposing that a contact is always between two fibres, we

find that the total number of contacts in a control volume is given by

$$n_b = \frac{1}{2}\left(\frac{l_f}{l_b} - 1\right)\frac{V\phi_s}{A_f l_f}. \tag{4.4}$$

If the fibres are sufficiently long compared to the distance between adjacent contacts, we can simplify this expression such that

$$n_b \cong \frac{1}{2}\frac{V\phi_s}{l_b A_f}. \tag{4.5}$$

For small sample sizes the standard deviation of the grammage of the analysed samples is large compared to the grammage difference between different samples. With these uncertainties in the calibration (for the density) of the gray scale values, we get quite large confidence bounds for both the solids contents and the average segment length. These uncertainties mean that direct comparison of results for different samples does not lead to a conclusive outcome. We therefore define a new parameter, the ratio of segment length to density, that seems to depend much less on the threshold gray value for solid used in the calibration.

Now we can define a parameter k such that

$$k \equiv \frac{\phi_s l_b}{z_0} = \frac{1}{a}\frac{\pi A_f}{2dz_0}, \tag{4.6}$$

where z_0 is an effective fibre width. It is evident from fig. (4.1) that this constant, when determined from a tomographic reconstruction of a sample of cardboard as in section 4.2, depends much less on the threshold used in the segmentation of the image than either $\frac{l_b}{z_0}$ or ϕ_s. With the introduction of parameter k and dividing eqn (4.5) by V we can express the contact density as

$$\frac{n_b}{V} \cong \frac{1}{2A_f z_0 k}\phi_s^2. \tag{4.7}$$

4.2 Model for paths along fibres in a fibre network

It is well known that in paper like deposited structures the fibres have predominantly planar orientation [14]. We can thus to a good approximation

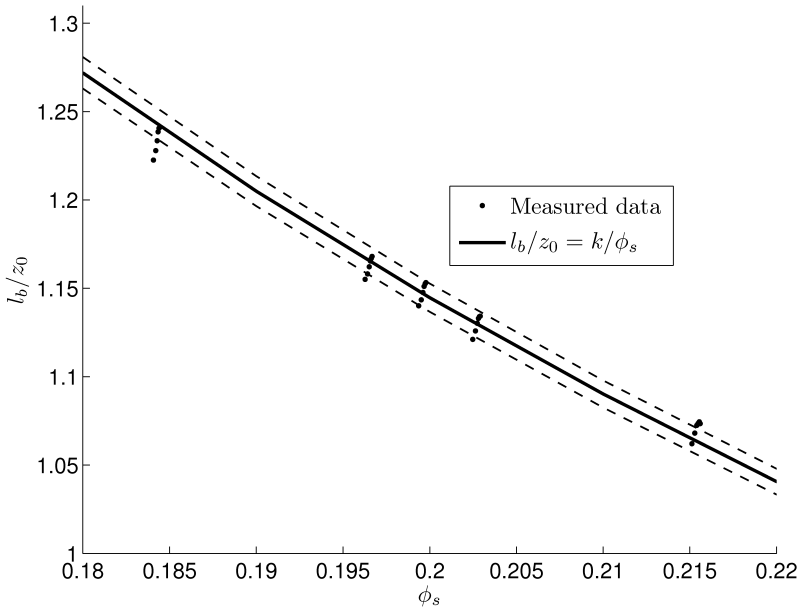

Fig. 4.1: $\frac{l_b}{z_0}$ plotted against ϕ_s for the tomographic data of sample 1. The five distinguishable groups of data are the results for different threshold gray scale values. The normalized standard deviation for k is about 1% (dashed line) which is less than a half of that for either ϕ_s or $\frac{l_b}{z_0}$.

assume that cardboard consists of stiff fibres that all lie along the xy-plane. The quintessential idea is that along a path through fibres in such a fibre network, the only z-displacements of the path appear at fibre-fibre contacts.

A contact at point i will lead to a point in the next fibre directly below the contact by an amount of z_i. Adjacent contacts are separated by a horizontal distance l_i (fig. (4.2)). The 3-d distance between two neighbouring contacts is thus given by

$$p_i = \sqrt{z_i^2 + l_i^2}. \tag{4.8}$$

To reach the target plane, we need to have a total z-displacement of d, where d is the distance between the two planes. The total displacement in

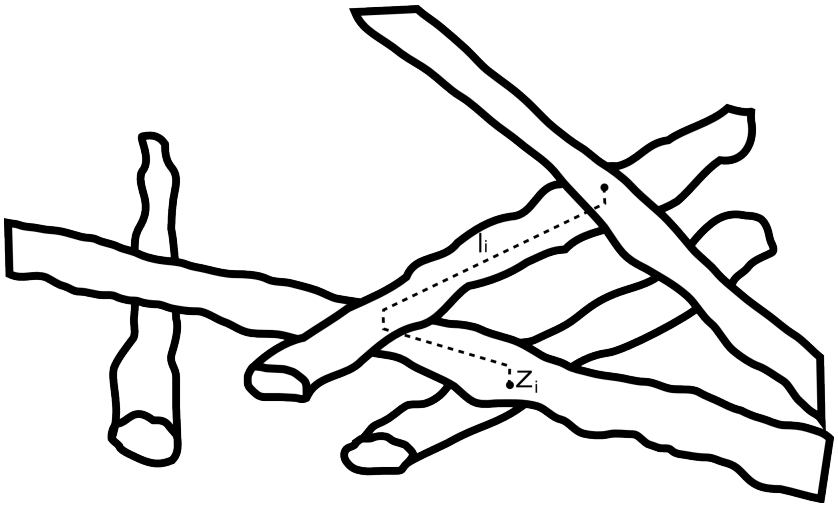

Fig. 4.2: If the z-orientation in the fibre network is negligible, the only displacements in the z-direction along a path through fibres appear at fibre-fibre contacts.

the z-direction is the sum of the displacements at contacts,

$$d = \sum_n z_i = n z_{\text{ave}}, \tag{4.9}$$

where n is the number of contacts along the path and z_{ave} is the average z-displacement at a contact. The total path length is given by

$$p = \sum_n p_i = n p_{ave} \tag{4.10}$$

Combining eqns (4.9) and (4.10), we find that

$$\frac{p}{d} = \frac{p_{\text{ave}}}{z_{\text{ave}}} = \frac{\sum_i \sqrt{l_i^2 + z_i^2}}{d}. \tag{4.11}$$

Now the problem is to derive the average distance between adjacent contacts, l_{ave}, from the measurable parameters p_{ave} and z_{ave}.

For each contact, we have assumed that the adjacent contact along a path is always on the other side of the fibre. For a uniform distribution along the length between adjacent contacts on one side of the fibre, the expected value for the distance to the nearest contact is $l_{\text{b1}}/4$ with l_{b1} the distance

between the adjacent contacts on the opposite side of the fibre. As described in sec. 3, the distribution of fibre segment lengths follows a Poisson process and is thus given by eqn.(3.10).

The probability that a contact is located between two adjacent contacts on the opposite side separated by distance l_{b1} is proportional to the distance l_{b1}. For long fibres we find that the probability for a point along the fibre to be located between two contacts on the opposite side separated by distance l_{b1} is given by

$$P(l_{b1}) = \frac{1}{\overline{l_{b1}}^2} e^{-\frac{l_{b1}}{\overline{l_{b1}}}} l_{b1}, \tag{4.12}$$

where $\overline{l_{b1}}$ is the mean distance between contacts on one side. Assuming a constant contact depth, z_0, we find that the expected value for p_i, i.e. p_{ave}, is given by

$$EV(p_i) = \int P(l_{b1}) p_i(l_{b1})\, \mathrm{d}l_{b1} = \int \frac{1}{\overline{l_{b1}}^2} e^{-\frac{l_{b1}}{\overline{l_{b1}}}} l_{b1} \sqrt{(\frac{l_{b1}}{4})^2 + (z_0)^2}\, \mathrm{d}l_{b1}. \tag{4.13}$$

With the substitution $y = \frac{l_{b1}}{z_0}$ we can write eqn (4.13) in the form

$$\frac{EV(p_i)}{z_0} = \int \frac{z_0^2}{\overline{l_{b1}}^2} e^{-\frac{z_0 y}{\overline{l_{b1}}}} y \sqrt{(\frac{y}{4})^2 + (1)^2}\, \mathrm{d}y. \tag{4.14}$$

The solution to this integral is shown in appendix A.2 and is of the form

$$\frac{EV(p_i)}{z_0}(x) = \frac{\pi}{2}\left(H_1(t) - \frac{t}{2}\left(H_0 - H_2 + \frac{t}{2\sqrt{\pi}\Gamma(\frac{5}{2})} \right) - tN_2(t) \right), \tag{4.15}$$

where $H_i(\beta\mu)$ are i order Struve functions and $N_i(\beta\mu)$ i order Neumann functions and $t = 4\frac{z_0}{\overline{l_{b1}}}$.

Assuming that all contacts can be divided into contacts on either the top or the bottom side of the fibre, we find that the number of contacts on one side of the fibre is

$$n_{\text{one side}} = \frac{l_f}{\overline{l_{b1}}} - 1. \tag{4.16}$$

Assuming that, on the average, fibres have an equal amount of contacts on both sides, we find that

$$n_{\text{bf}} = \frac{l_{\text{f}}}{l_{\text{b}}} - 1 = 2n_{\text{one side}} = 2\left(\frac{l_{\text{f}}}{\overline{l_{\text{b1}}}} - 1\right). \tag{4.17}$$

Solving for l_b and assuming long fibres we find that the average segment length for the fibre network is

$$l_b \cong \frac{1}{2}\overline{l_{\text{b1}}}. \tag{4.18}$$

4.3 Non-planar fibre networks

If the fibres of the network are flexible or have a non-zero orientation in the z-direction, segments of fibres are not strictly planar. Let us assume that this can effect be described by a mean segment angle in the z-direction. This means that, assuming that the shortest path does not contain any backward going segments, the z-displacement along the path is larger than z_0. This effective z-displacement fig. (4.3) can be expressed in the form

$$z_{i,\text{eff}} = l_i \sin\alpha + z_0 \cos\alpha. \tag{4.19}$$

The expected value for this effective displacement using the same segment length distribution as in eqn (4.12) is given by

$$EV(z_{\text{eff}}) = \int \frac{1}{\overline{l_{\text{b1}}}^2} e^{-\frac{l_{\text{b1}}}{\overline{l_{\text{b1}}}}} l_{\text{b1}} \left(\frac{l_{\text{b1}}}{4}\sin\alpha + z_0\cos\alpha\right) \mathrm{d}l_{\text{b1}} = \overline{l_{\text{b1}}}\frac{\sin\alpha}{2} + \cos\alpha z_0. \tag{4.20}$$

When determining $\frac{p}{d}$ from the measured paths, we are actually measuring $\frac{p_{ave}}{z_{\text{eff}}}$. Rearranging we find that

$$\frac{p_{\text{ave}}}{z_0} = \frac{p_{\text{ave}}}{z_{\text{eff}}}\left(\cos\alpha + \frac{\overline{l_{\text{b1}}}\sin\alpha}{2z_0}\right). \tag{4.21}$$

This results in an overestimation of the density of contacts if the fibrous network consists of flexible fibres or if the fibres have an orientation in

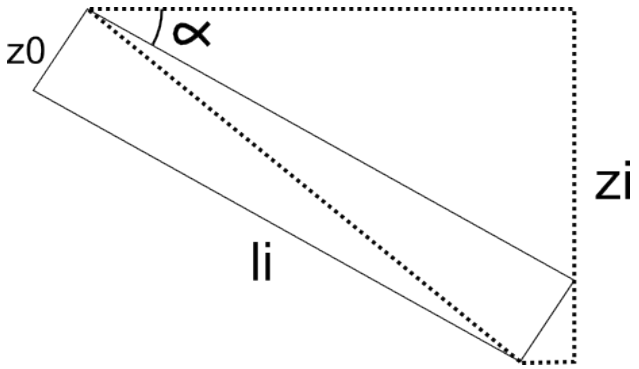

Fig. 4.3: Z-displacement in the case of a flexible fibre.

the z-direction, see fig. (4.4). There are many inaccuracies in this kind of estimation, e.g., it is not reasonable to assume that the shortest path will continuously propagate towards the target plane. If a contact leads to an inclined fibre then on the average a half of the nearest contacts lie in a direction opposite to the propagation direction. Even so, assuming that this kind of average angle approach is valid, it is not clear how the angle α could be determined.

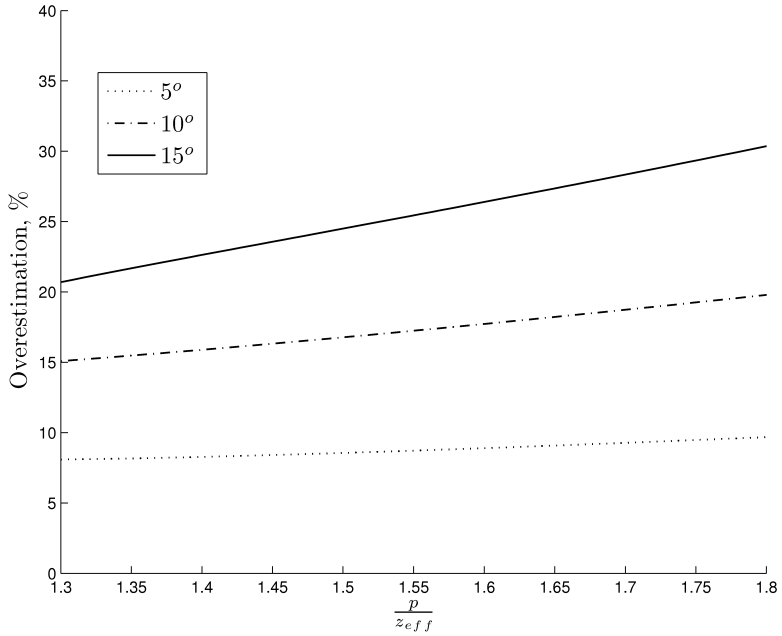

Fig. 4.4: Overestimation of the contact density as a function of the ratio p/d when the fibres are assumed stiff and planar if the segments are inclined by an angle of 5^o, 10^o and 15^o. If the fibres are flexible or have an orientation in the z-direction the assumption that the only z-displacements of the shortest path appear at fibre-fibre contacts does not apply.

5. IMAGE PROCESSING

Reconstructed tomographic images may not be as such suitable for analysis. The sample holder is for instance always a bit inclined and the cardboard sample is therefore not straight. Raw tomographic images are also often quite noisy, and this can lead to inaccurate analysis if not dealt with. One of the more problematic challenges when using tomographic images is the calibration of gray scale values for getting the true material density. There are various factors that contribute to this problem including use of polychromatic light, source stability and various artefacts. This is a known problem in x-ray tomography. For instance, in medical science it is common to use a phantom in tomographic imaging, i.e., an object with known material densities and absorption properties similar to those of the sample analysed. The image of the phantom can be used to more accurately identify material components in the reconstructed image of the sample. Using a phantom in the case of paper-like materials is a method worth considering in the future, because it could easily result in a more accurate estimation of the density of the imaged samples.

5.1 Image analysis

The reconstructed tomographic images were filtered for noise reduction using a method based on the variance of the local gray scale values [5]. This method measures first the standard deviation (variance) of gray scale values in a region of chosen size to be filtered. The performed smoothing of that region depends on the measured variance so that, if it is large compared to a set threshold that corresponds to the variance related to

random noise, the smoothing of gray scale values is small, and vice versa. The result of this kind of filtering is that edges do not become blurred, but the noise in homogeneous areas is reduced. The filtered images were rotated manually so that the imaged cardboard lay in the xy-plane. From the processed image a region was cropped from the middle of the sample so that the selection did not include any cut marks, bended edges or other unwanted features.

The top and bottom surfaces were determined using the Carpet program [1], which is a program that lets a flexible surface ascend on the image. To reduce the effect of pinholes the parameters, viz., driving force and surface tension of the surface were chose so that the ascending plane was relatively stiff. The number of iterations was chosen large enough to make sure that the carpet will find its equilibrium position. The planes, in which between the image analysis was made, were chosen by averaging the surface determined using the carpet program. These planes are specified in tables C.1 and C.2.

5.2 Calibration

For calibrating the gray scale values of the tomographic images, we concluded that the most reliable measurement on the samples is their area density, more commonly known as the grammage. The underlying idea is that, using grammage as the reference value, we can assign a real density to each gray scale value. Grammage (ρ_{A}) is defined as the mass of a square meter of cardboard,

$$\rho_{\mathrm{A}} = \frac{m}{A} = \frac{V_{\mathrm{s}}\rho_{\mathrm{f}}}{A}, \tag{5.1}$$

where V_{s} is the total volume of fibres, ρ_{f} is the density of the cell wall and A the area of the analysed sample. For a binary image we find that

$$\rho_{\mathrm{A}} = \frac{\phi_{\mathrm{s}} V s^3 \rho_{\mathrm{f}}}{A s^2}, \tag{5.2}$$

where ϕ_{s} is the solids content of the image, V and A are the volume and area of the image in voxels and pixels, respectively, and s is the pixel size.

Simplifying eqn (5.2) we find that the grammage can be expressed as the sum of the grammage for separate slices,

$$\rho_{\mathrm{A}} = \sum_i \phi_i s \rho_{\mathrm{f}}, \tag{5.3}$$

in which ϕ_i is the solids contents of the ith xy -plane. Assuming now that the average cell wall density is the same for all samples, we get an individual threshold T for every tomographic image. Based on the literature [14], we chose a cell wall density of 1500 kg/m^3. Thresholding each image separately by using the corresponding threshold T, we can determine $\rho_{\mathrm{A}}(T)$.

The standard deviation of the grammage for a sample of area A is given by [14]

$$\sigma_\rho = \frac{\sqrt{N} m_{\mathrm{f}}}{A} = \frac{\sqrt{\frac{\rho_{\mathrm{A}} A}{\mathrm{f}}} m_{\mathrm{f}}}{A} = \sqrt{\frac{\rho_{\mathrm{A}} m_{\mathrm{f}}}{A}}. \tag{5.4}$$

The fibre coarseness and length of the samples were estimated to be 0.25 µg/m and 2 mm, respectively. An example of thresholding is shown in fig. (5.1). The maximum and minimum threshold values, $T_{\max}$ and $T_{\min}$ were chosen such that $\rho_{\mathrm{A}}(T_{\max}) < \rho_{\mathrm{A}} - \sigma_{\rho_{\mathrm{A}}}$ and $\rho_{\mathrm{A}}(T_{\min}) > \rho_{\mathrm{A}} + \sigma_{\rho_{\mathrm{A}}}$ (tables C.4 and C.5). For the first two sets of samples, three additional values were chosen near the value of mean grammage.

There were three reasons for why we chose to use binary images for the calibration. Fist of all, the gray scale values of the reconstructed images do not depend linearly on the density. Therefore the benefit of the additional information preserved by not thresholding is questionable. Secondly, even if the gray scale values would be accurately calibrated, we would still have the problem of thresholding. The third reason was that the gray scale value of voids in the image contribute to the sum of the gray scale values. Because of imaging artefacts, the local mean gray scale value of the void is not constant over the image, it is relatively small near fibres and relatively large in areas away from any fibres. Owing to this, subtraction of the gray value from that of the void requires information about the sample that cannot be directly measured.

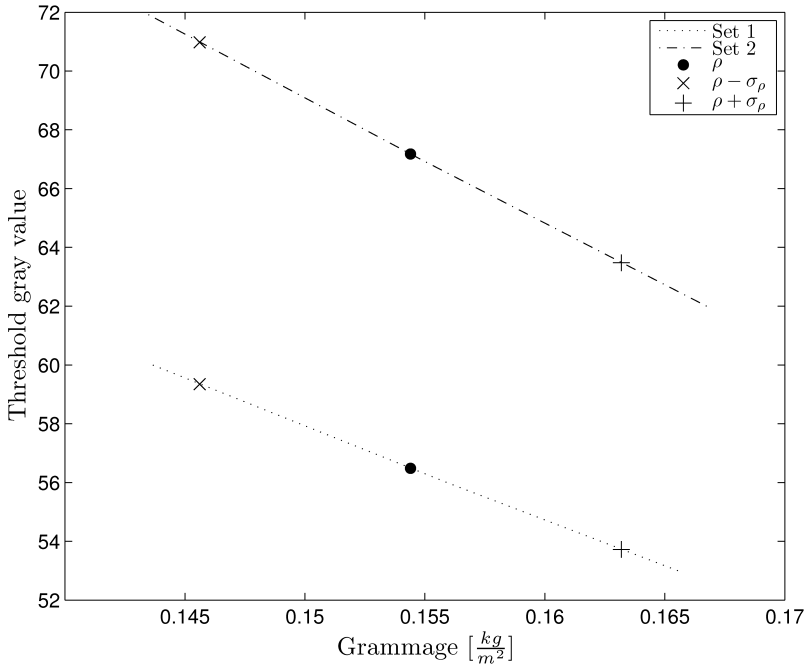

Fig. 5.1: Threshold gray value against grammage for sample 1. Because 8-bit images were used, the results were interpolated linearly between data points.

5.3 Distance transform

Distance transforms are operators normally applied to binary images. The result of such a transform is a representation, where a chosen set of foreground pixels (2D) or voxels (3D) have the value of the shortest distance to a chosen object. In this case, the object is chosen to be the voxels in an xy-plane, which belong to the solid phase in the image. In other words, the distance transform is applied so that every voxel representing fibres in the cardboard is assigned a value that is the length of the shortest path along the fibre network to the target plane.

Chamfer distance transforms are commonly used to approximate Euclidian distances. They are based on the approximation that the chosen distance for a given voxel can be computed from those of its neighbours. A

Chamfer mask can be defined as a set of weighted legal displacements for a voxel, in this case displacements leading to voxels representing fibres. Such masks are represented in fig. (5.2). The Chamfer distance between two voxels is then the smallest sum of the possible weighted displacements that can be used to connect the voxels. To approximate the Euclidian distance one has to scale the Chamfer distance. Usually the scale is taken to be the same as the weight in the directions of the unit vectors but optimization requires the minimization of the error in respect to both the Chamfer weights and the scale factor [15].

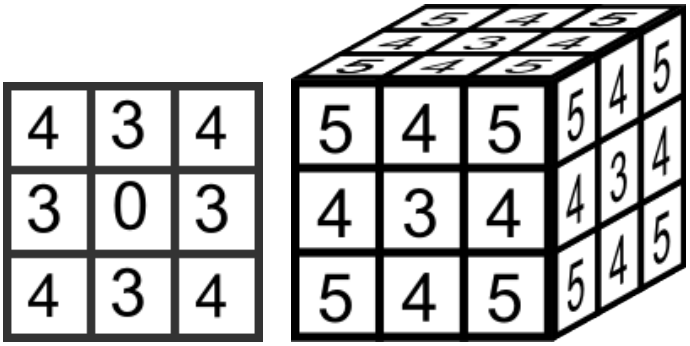

(a) 2D Chamfer mask (b) 3D Chamfer mask

Fig. 5.2: Chamfer masks for two and three dimensions. The starting voxel is located in the center and the values represent the Chamfer distance from the center to the neighbouring voxels.

Starting from the solid phase voxels of the chosen plane, the algorithm assigns to all of its legal neighbours the corresponding value of the Chamfer mask plus the value of the starting voxel, fig. (5.3). If the assigned value is smaller than the value that already exists in the voxel, the existing value is replaced by the new assigned value. Solid phase voxels without a value assigned to them are considered to have an infinite value.

As a result of this procedure for a binarized tomographic image, we find a distance map, where every voxel has a value that represents its Chamfer distance to the target plane along the fibre network. With the chosen mask, the approximate Euclidian distance is one third of the sum of the weighted displacements.

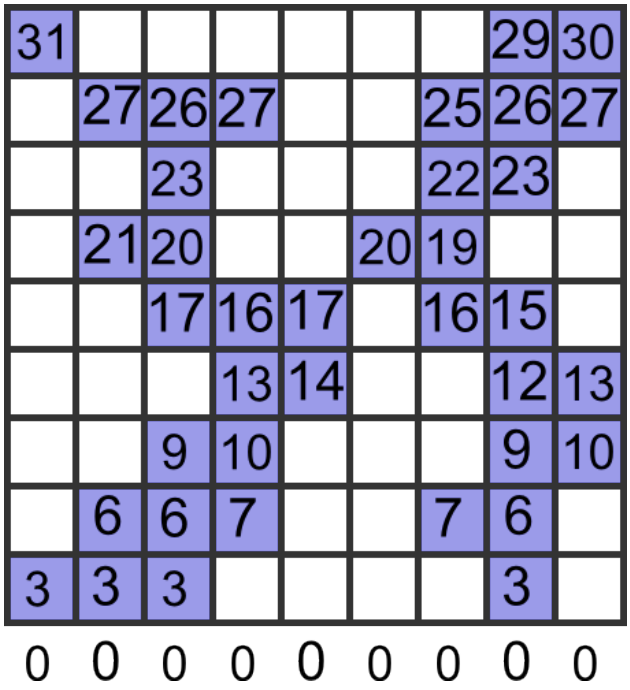

Fig. 5.3: An illustration of the distance transform on a 2D image. The solid phase pixels (voxels) are shaded and the object is represented as a row of zeros at the bottom. The Chamfer distance to a pixel is the smallest sum of weighted displacements (fig. (5.2(a))) that connects it to the object.

6. EXPERIMENTAL METHODS

Tomographic images allow for a detailed analysis of the cardboard structure. After careful calibration of the gray scale values, different samples can be compared with one another. It is possible to do many analyses based on the tomographic reconstructions. These include density profiles, pore structure and surface roughness. In this work analysis is focused on the contact densities and the density profiles.

6.1 Cardboard samples

The cardboards analysed comprised eight samples. These samples were all manufactured in the same way and with the same pulp, but contained different additives. The known characteristic parameters of the samples are shown in table B.1. Notice that even though all the samples have a similar grammage, their apparent densities and z-strengths vary appreciably. When the z-strength is plotted against apparent density, most of the samples fall on the same curve, but samples 2,3 and 4 do not follow from this trend as is evident from fig. (6.1).

6.2 Measurements

All the sample sets were cut from the cardboards and imaged with an Xradia Micro-XCT-400 using a magnification of 10x or 4x. The imaging parameters are shown in table (6.1). After reconstruction, the resulting tomographic images had a voxel size of 2.2 μm (10x) or 2.5 μm (4x). The

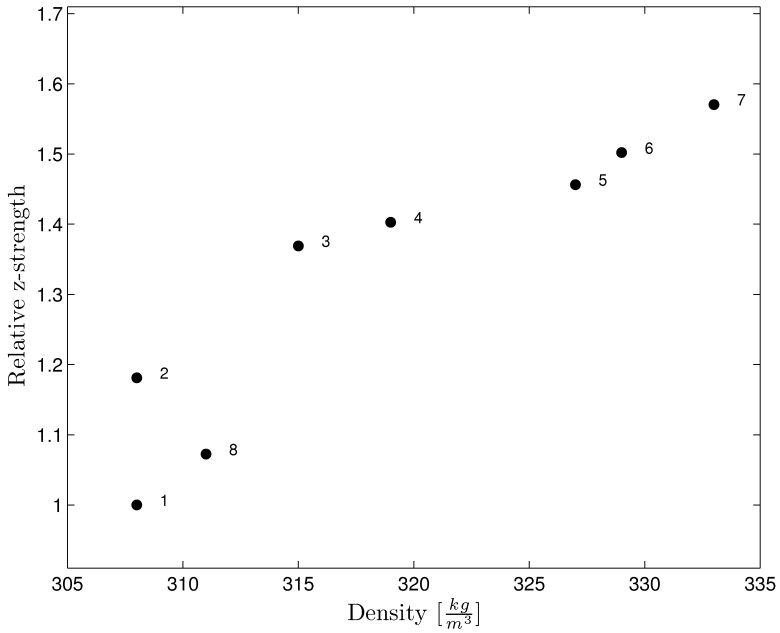

Fig. 6.1: Measured relavite z-strength agaist apparent density for the analysed cardboard samples. Samples 2,3 and 4 do not follow the trend shared by the other samples.

size of the portion of the tomographic images suitable for analysis, i.e., the part of the image not containing any cuts or bends from sample preparation, was about 1 mm^2 (10x) or 14 mm^2 (4x).

6.2.1 Density profiles

The density profile, or more accurately the solids content profile, of the cardboard samples was determined by measuring the solids content ϕ_s, separately for each cross section of the thresholded tomographic images. The profile was determined between two planes determined by the carpet program as the top and bottom surfaces of the samples. The profiles for all the samples studied are shown in appendix D.1. The threshold value used in the binarization of the tomographic images was chosen using the mean grammage of the cardboard as a reference.

Tab. 6.1: Imaging parameters for the sample sets

set #	1	2	3	4
Magnification	10x	10x	4x	4x
Tube voltage [kV]	20	20	20	20
Exposure time [s]	90	90	20	20
Number of projections	745	745	1189	1981
Voxel size [μm^3]	2.1974^3	2.1974^3	2.5138^3	2.5138^3

For all the density profiles in the z-direction, four quantitative features were determined: mean solids content, ϕ_s, variance, σ_{ϕ_s}, slope and curvature. The slope was taken from the derivative of a first order polynomial least-squares fit. The curvature was taken from the second derivative of a second order polynomial fit. The results are shown in the appendix D.1 (tables D.1, D.2, D.3 and D.4).

6.2.2 Contact density

Because the solids content is not equal in the top and bottom layers, the shortest path is not an injective function. This means that the distribution of shortest paths from top to bottom is not equal to the distribution from bottom to top. It depends on the solids content in the planes considered.

Let us assume that we have planes A and B such that $\phi_{sA} < \phi_{sB}$. Now the shortest paths from B to A will include all the paths from A to B because they are the shortest paths between these planes. The remainder of the paths will by definition be longer than any of the paths from A to B. Because of this dependence on the chosen planes, the distance transform for the images of sets #1 and #2 was also taken from the two nearest planes to the ones that were determined using the carpet program (tables C.2, C.1). There were no significant differences between the results for the planes determined by the carpet algorithm and the neighbouring planes.

The constant $k(i)$ in eqn (4.7) was determined as an average over both propagation directions using the mean solids content in the cross sections

between the starting plane and plane i, and the mean shortest path between these planes,

$$2k(i) = \left(l_{\mathrm{b}} \left(\frac{p_i}{i} \right) \frac{\sum_{j=1}^{i} \phi_{\mathrm{s}_j}}{i} \right)_{top \to bottom} + \left(l_{\mathrm{b}} \left(\frac{p_i}{i} \right) \frac{\sum_{j=1}^{i} \phi_{\mathrm{s}_j}}{i} \right)_{bottom \to top} , \tag{6.1}$$

where $l_{\mathrm{b}} \left(\frac{p_i}{i} \right)$ is the inverse function of eqn (4.15). Examples of the values of $k(i)$ are shown in fig. (6.2). The shape of these curves is likely to result from the behaviour of the fraction of bonded crossings as a function of sample thickness d. For a fibre network of thickness d, there is a distance from the surface, d_0, where all the fibres are completely within the sample and the structure of the network in this region is not affected by surfaces. This means that, if we denote the total thickness by $d = x + 2d_0$ and let x increase, the number of contacts should increase proportional to x, and we find that

$$\frac{\partial n_{\mathrm{b}}}{\partial x} = \frac{\partial}{\partial x} a(x) \frac{2\phi^2 A (2d_0 + x)^2}{\pi A_{\mathrm{f}}^2} = C \qquad ; x > 0 \tag{6.2}$$

with C an undetermined constant. This equation can easily be solved for $a\,(x)$:

$$a(x) = \left[\frac{C}{D} x + C' \right] \frac{1}{(x + 2d_0)^2} , \qquad D = \frac{2\phi_{\mathrm{s}}^2 A}{\pi A_{\mathrm{f}}^2} , \tag{6.3}$$

in which C' is another undetermined constant. The parameter k was defined in eqn (4.6) such that

$$k = \frac{\phi_{\mathrm{s}} l_{\mathrm{b}}}{z_0} = \frac{\pi A_{\mathrm{f}}}{2adz_0}. \tag{6.4}$$

Substituting in this expression the $a = a\,(x)$ of eqn (6.3) with $x = d - d_0$, we find that

$$k = \frac{\phi_{\mathrm{s}}^2 A}{z_0} \frac{d}{C(d - 2d_0) + C/D} \qquad ; d > 2d_0. \tag{6.5}$$

It is evident from fig. (6.2) for the k determined by image analysis from the tomographic image of sample 6, that the function eqn (6.5), assuming that $d_0 > \frac{1}{2D}$, describes quite well the numerically determined behaviour.

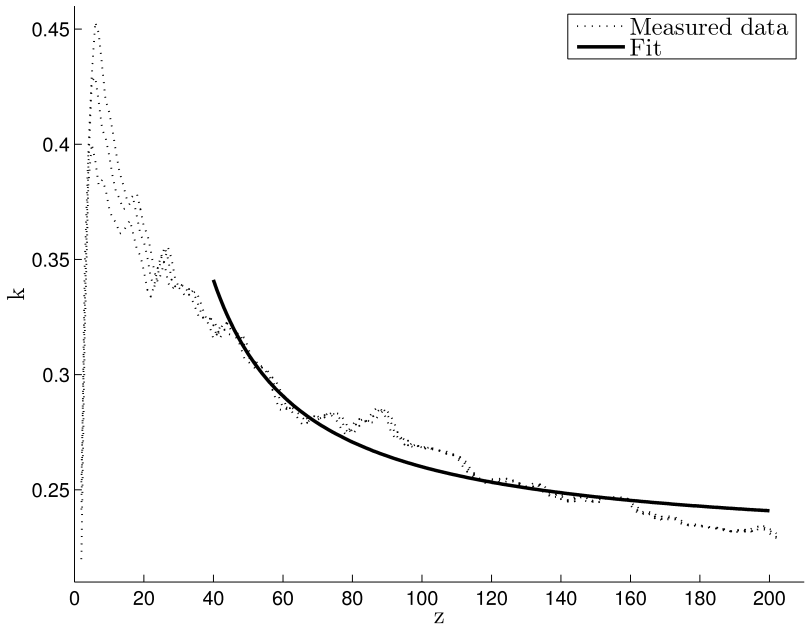

Fig. 6.2: k as a function of distance z between the chosen planar surfaces (planes) for sample 6 from set 2, with a threshold gray scale value of 57 for the planes determined using the carpet program and for their nearest planes. It is evident that the effect of how the planes are chosen is noticeable only for small values of z. The solid line is a fit by eqn (6.5) for the values of z greater than 40.

The values for k were determined as averages over the different threshold values used, tables C.4 and C.5. The results are shown in table D.5.

6.3 Results

6.3.1 Shortest path analysis

When the contact densities for all the samples are plotted against solids content, all the data seem to fall on a single curve, fig. (6.3). The constant k was similar for all samples with a 3% standard deviation of the mean, and the contact density (n_b/V) seems to be proportional to the square of the solids content. This is in agreement with earlier work on fibrous materials. In a study of the compressibility of wool, van Wyck [19] derived an expression for mean length between contacts for nonplanar networks,

$$l_b = \frac{2V}{\pi w_f n_f l_f} = \frac{2A_f}{\pi w_f}\frac{1}{\phi_s}. \tag{6.6}$$

Using the same assumptions of long fibres as in section 4, the contact density can in this case be expressed in the form

$$\frac{n_b}{V} = \frac{\pi w_f}{4A_f^2}\phi_s^2. \tag{6.7}$$

Similar relations between density and contact density is found also in other work. Deng [3] mentions that Komori and Makashima also found a similar relation while taking into account the flattening effect of orientation under compression. Corte and Kallmes derived the contact density for multiplanar sheets which consist of stacks of two dimensional sheets [11].

In van Wyck's model, the product $l_b\phi_s$ is a constant that depends solely on fibre geometry. This would be true also for the presented model if the product ad could be expressed as a function of fibre geometry. As seen from eqn(6.3), the required relation that $a \propto d^{-1}$ is fulfilled if $d >> 2d_0$ and $d^2 >> C'$. If this is the case, the implication is quite notable. It would mean that the contact density is coupled with the density of the fibrous network in a rather strong manner, depending only on the geometry of the fibres. The result, that different additives seem to alter the density of the cardboard samples but not the constant k, supports this theory. Koubaa

and Koran found a similar result [12] when measuring the internal bond strength of paper. Papers made from the same type of pulp all fell roughly on the same curve when their z-strength was plotted against the apparent density, but differences between different kinds of pulp were noticeable.

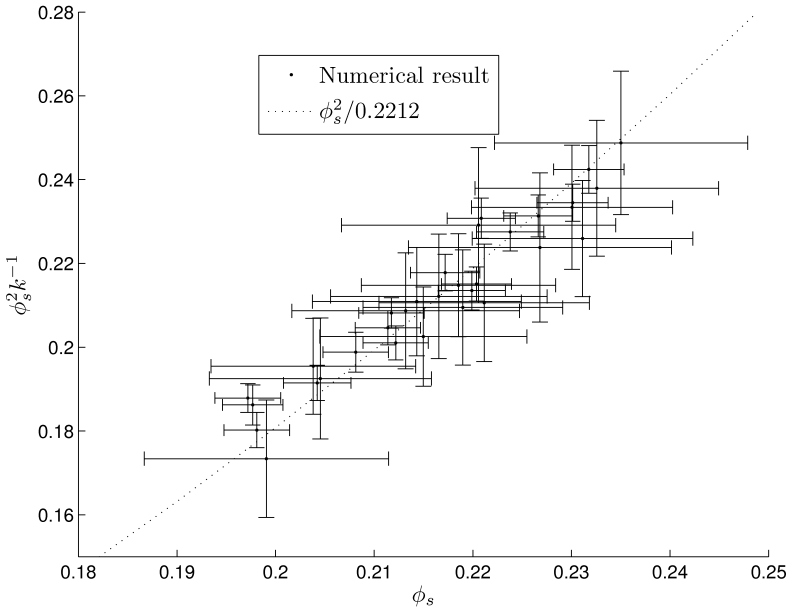

Fig. 6.3: $\phi_s^2 k^{-1}$ plotted against solids content ϕ_s for all sample sets. The values measured for k were quite similar for all the samples, with a 3.1% standard deviation of the mean.

Although both the contact densities (fig. (6.3)) and the average segment lengths (fig. (6.4)) as measured here seem to support the proposed model, it is worth mentioning that the ranges of their values were quite narrow.

6.3.2 Density profiles

Most noticeably, the differences in the density profiles between small samples from the same run is quite significant. This implies that the internal differences in cardboard sheets do not only appear in the grammage, but

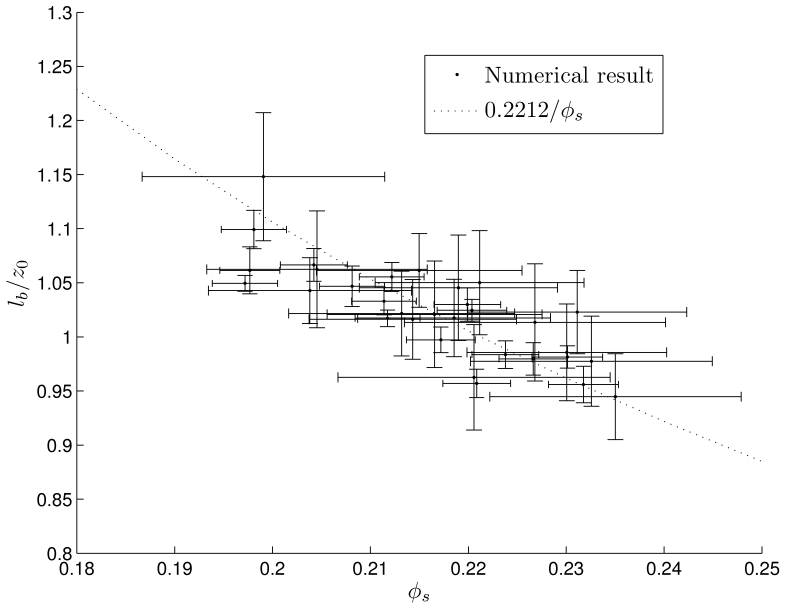

Fig. 6.4: l_b/z_0 plotted against solids content ϕ_s for all sample sets.

there are also noticeable structural differences. There is as well a significant discrepancy between the measured apparent density and the solids contents determined from the tomographic images. Most significantly the tomographic images of the sparse samples, 1 and 8, have a lower solids content than the measurements for the apparent density indicate. Secondly, the apparent densities of samples 1 and 2 are the same, a result that has not been observed in any of the tomographic images.

The amount of samples analysed is too small to make reliable conclusions based on the density profiles, but there are still some observations worth mentioning. All the solids contents profiles have a slope in the same direction: teh samples were denser at the bottom surface. A second observation is that densification seems to occur at both surfaces. Also, the denser is the sample, the larger is the curvature of the profile, see fig. (6.5).

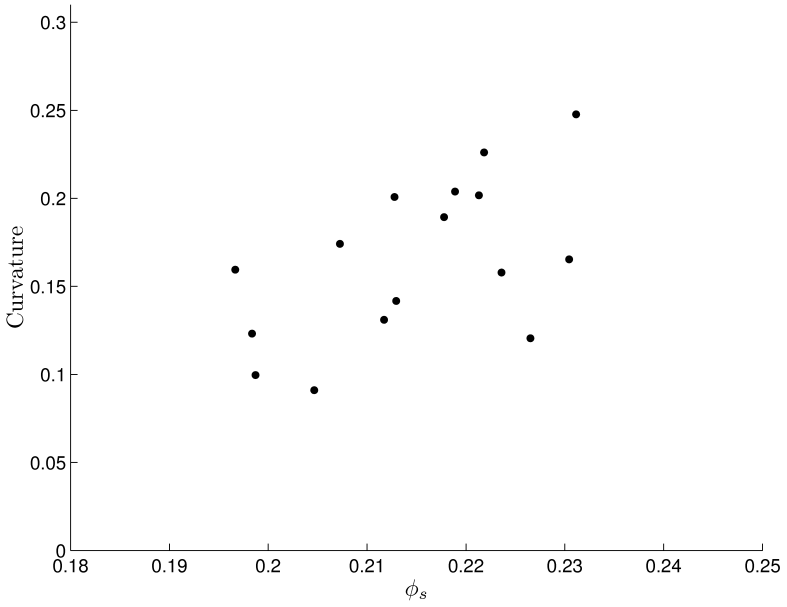

Fig. 6.5: The curvature of the density profile plotted against the mean solids content of the sample.

6.3.3 Correlation between the contact densities and measured z-strength

For the z-strength of cardboard we chose the results from a z-directional tensile strength test. This strength is suitable for describing the internal bond strength [12], and is not so dependent on the planar fibre orientation as, e.g., the result of the Scott-bond test [2].

There is an evident lack of theoretical models for paper strength in the out-of-plane direction. However, there have been reports of relationships between different strength properties of paper [16], between in-plane tensile strength and z-strength in particular.

The one of the most widely used equations related to the strength of a fibre network is the Page equation [3]

$$\frac{1}{T} = \frac{9}{8Z} + \frac{A_f \rho_f g}{b P l_f R B A}, \tag{6.8}$$

where T and Z are the finite-span and zero-span tensile strength, respec-

tively, both expressed as a breaking length, A_f is the fibre cross-sectional area, g the gravitational acceleration, b the bond strength, P the fibre perimeter, l_f the fibre length and RBA the relative bonded area. The Page equation is not suitable for describing the z-strength because of the assumptions made in the fibre orientation, but it gives a good idea of what the underlying factors are. For an isotropic network, the tensile strength is governed by the fact that, in breaking at a fibre level, either a fibre segment or a fibre-fibre bond must fail. Out-of-plane strength is generally a few orders of magnitude less than fibre strength, and it is thus unlikely that the stresses would be large enough for fibre failure to be of importance. We can safely assume that, for a planar network, the out-of-plane strength is controlled by the bond strength.

This means that the tensile strength of cardboards should depend strongly on RBA and thus also the number of bonds, because as

$$RBA = \frac{n_b A_b}{n_f A_{tot}} \propto \frac{n_b}{V} \frac{1}{\phi_s}, \tag{6.9}$$

where A_b is the average area of a bond between two fibres and A_{tot} is the average surface area of a fibre. Neglecting the effect of the zero-span tensile strength from eqn(6.8) and expressing it in the form of z-strength (σ_z) as a function of contact density, eqn(4.7), we find that

$$\sigma_z \propto \frac{\phi_s^2}{k}. \tag{6.10}$$

The results are shown in fig. (6.6). It seems that the measured z-strengths of the cardboard samples satisfy quite well the relationship eqn (6.10).

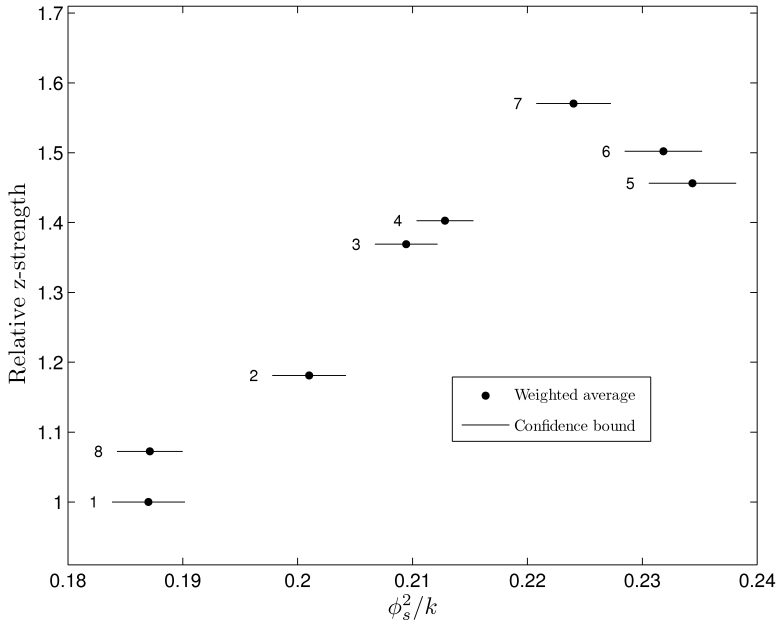

Fig. 6.6: Z-strength of cardboard samples plotted against $\phi_s^2 k^{-1}$ using the weighted mean of the measuremed values as the data points (table D.7).

7. CONCLUSIONS AND DISCUSSION

It seems that the contact density of a fibrous network, determined in the way introduced in this work, seems to be proportional to the square of the solids content. The observation is in agreement with earlier theoretical models for fibrous materials. Different additives do not seem to affect the connectivity independent of the network density as the relation between solids content and contact density was similar for all samples regardless of the additives used.

The parameter k defined above because of the reliability of its determination from tomographic images, which describes the intrinsic connectivity of the material in terms of the fraction of bonded crossings a, seemed to be relatively constant over the whole set of samples with a 3.1% standard deviation of the mean. This means that the contact density is governed by the manner by which the network is formed, and this explains why additives do not affect independently the density and the contact density of cardboard.

In summary, there are three different factors of the raw materials that contribute to the structure of the network: geometric properties, flexibility and additives. For the geometric properties, the most prominent is the ratio between the area of the fibre cross-section and the fibre perimeter, a property that has already been noted in previous studies [7]. This is obvious, because assuming fibres do not collapse, networks formed with fibres with thick cell walls will have a higher density than a similar network consisting of fibres with the same perimeter but a thinner cell wall.

Increasing the flexibility of the fibres will increase both the contact density and the sheet density [13]. In chapter 3 we derived the upper bound for

the number of contacts in a flexible three-dimensional network.

The effect of the additives is consistent with the known behaviour of fibrils and fines in papermaking. During the wet state of sheet formation fibrils and fines fill spaces between fibres making bridges of bound water. This increases the number of bonds formed during dewatering by increasing the Campbell forces [18], i.e., the surface tension forces pulling fibres together. This will also compress the structure in the z-direction making the sheet denser.

This result is important in practical applications. All the methods that increase the out-of-plane strength of cardboard by increasing the contact density of the sheet will result in a denser structure. It means that, in order to obtain strong cardboard with large bulk (low density), one has to be able to produce strong fibre-fibre bonds rather than many contacts.

From the density profiles we could conclude that differences between samples of the same cardboard were quite large for small sample sizes. This indicates that, for more reliable results, one should analyse either larger or a greater amount of samples. All the density profiles analysed here had a slope in the same direction with similar steepness. This means that the cardboards samples were all denser at the bottom regardless of the additives. Densification seems to have occurred at sample surfaces. This was indicated by larger curvature of the density profiles of denser samples. We cannot elaborate more on the densification results without knowing the actual density or grammage of the imaged samples. This problem could possibly be resolved by using a phantom when imaging the cardboards or by imaging several samples simultaneously.

The most obvious inaccuracy of the method still lies in the binarization of the images. It is also questionable if a simple threshold is sufficient for binarizing the images, as artefacts such as beam hardening and phase contrast alter the gray values of the fibres. While the use of a phantom could allow for more exact calibration it does not solve all the problems.

The model for the shortest path is also a bit simplified. It assumes that the shortest path is a sum of the shortest paths to the nearest fibres. This is

not necessarily the case, as combinations of longer segments can lead to a shorter overall path.

The approximation of planar fibres also causes some error as was seen in section 4. Although a way to correct for this error was introduced through an effective z-displacement, it is unclear how to determine an appropriate bending angle for the fibres. It is also unclear how important this correction is for the samples imaged are but, e.g., a z-orientation of 5^o results in an overestimation of the contact density by about 10% if the fibre network is assumed planar.

BIBLIOGRAPHY

[1] G. Chinga-Carrasco, H. Kauko, M. Myllys, J. Timonen, B. Wang, M. Zhou, and J. O. Fossum. New advances in the 3D characterization of mineral coating layers on paper. *Journal of Microscopy*, 232:212–224, 2008.

[2] J. M. Considine, D. W. Vahey, R. Gleisner, A. Rudine, S. R. du Roscoat, and J.-F. Bloch. Z-direction fiber orientation in paperboard. *Tappi Journal*, 34:25–32, 2010.

[3] M. Deng. *Paper, An Engineered Stochastic Structure*. TAPPI Press, Atlanta, 1994.

[4] L. A. Feldkamp, L. C. Davis, and J. W. Kress. Practical cone-beam algorithm. *Optical Society of America*, 1:612–619, 1984.

[5] R. C. Gonzales and R. E. Woods. *Digital Image Processing*. Prentice-Hall, Inc, New Jersey, 2nd edition, 1993.

[6] I. S. Gradshteyn and I. M. Ryzhik. *Table of Integrals, Series, and Products*. Academic Press, London, 1965.

[7] J. He, W. J. Batchelor, and R. E. Johnston. An analytical model for number of fibre-fibre contacts in paper and expressions for relative bonded area (RBA). *Journal of Material Science*, 42:522–528, 2007.

[8] G. T. Herman. *Fundamentals of Computerized Tomography*. Springer, London, 2nd edition, 2009.

[9] A. C. Kak and M. Slaney. *Principles of Computerized Tomographic Imaging* . IEEE PRESS, Electronic copy, 1999.

[10] O. Kallmes and O. Corte. Structure of paper I. The statistical Geometry of and Ideal Two Dimensional Fiber Network. *TAPPI*, 43:737–752, 1960.

[11] O. Kallmes and O. Corte. Structure of paper II. The statistical Geometry of a Multiplanar Fiber Network. *TAPPI*, 43:737–752, 1960.

[12] A. Koubaa and Z. Koran. Measure of the internal bond strength of paper/board. *Tappi Journal*, 78:103–111, 1995.

[13] J. Mäkinen. *The Mechanical and Geometrical Properties of Fibrous Structures*. PhD thesis, Department of Physics, University of Jyväskylä, 2001.

[14] K. Niskanen. *Paper Physics*. Fapet Oy, Jyväskylä, 1998.

[15] E. Remy and T. E. Optimizing 3D chamfer masks with norm constraints. In *Int. Workshop on Combinatorial Image Analysis, Caen, France*, pages 39–56, 2000.

[16] S. P. Singh. Relationship of z-tensile strength with in-plane strenght properties of paper. *Indian Journal of Chemical Technology*, 14:317–320, 2007.

[17] H. Turbell. *Cone-beam reconstruction using Filtered Backprojection*. PhD thesis, Institute of Technology, University of Linköping, 2001.

[18] A. K. Vainio and H. Paulapuro. Interfiber bonding and fiber segment activation in paper. *BioRecources*, 2:442–458, 2007.

[19] C. van Wyck. Note on the compressability of wool. *The Journal of The Textile Industry*, 34:285–292, 1946.

[20] J. A. Åström, J. P. Mäkinen, H. Hirvonen, and J. Timonen. Stiffness of compressed fiber mats. *Journal of Applied Physics*, 8:5056–5061, 2000.

Appendices

Appendix A

DERIVATION OF FORMULAE

A.1 The fraction of contacts for flexible fibres.

Substituting eqn (3.3) into eqn (3.13) we find that

$$a_{\text{flex}} = \sum_{n=2}^{\infty} \frac{\overline{c}^n 2(n-1)!}{n!n!(e^{\overline{c}} - \overline{c} - 1)} = \frac{2}{e^{\overline{c}} - \overline{c} - 1} \sum_{n=2}^{\infty} \frac{\overline{c}^n}{nn!}, \tag{A.1}$$

The exponential integral can be expressed as a series

$$\text{Ei}(x) = \gamma + ln|x| + \sum_{n=1}^{\infty} \frac{\overline{c}^n}{nn!}, \tag{A.2}$$

where γ is the Euler-Mascheroni constant. Rearranging we can write eqn (A.2) in the form

$$\sum_{n=2}^{\infty} \frac{\overline{c}^n}{nn!} = \text{Ei}(x) - \gamma - ln|x| - x. \tag{A.3}$$

By substituting the sum in eqn (A.1) we find that

$$a_{\text{flex}} = \frac{2}{e^{\overline{c}} - \overline{c} - 1} \left[\text{Ei}(\overline{c}) - ln(\overline{c}) - \overline{c} - \gamma\right]. \tag{A.4}$$

A.2 The expected value of the path between adjacent contacts.

With the substitution $\frac{y}{4} = x$ and $4\frac{z_0}{l_{c1}} = t$ into eqn (4.14) we get

$$(x) = t^2 \int_0^{\infty} xe^{-tx} \sqrt{x^2 + 1}\, \mathrm{d}x. \tag{A.5}$$

This can be written as a partial derivative with respect to t such that

$$\frac{EV(p_i)}{z_0}(x) = t^2 \frac{\partial}{\partial t} \int_0^\infty -e^{-tx}\sqrt{x^2+1}\,\mathrm{d}x. \tag{A.6}$$

From [6] we know that

$$\int_0^\infty \frac{xe^{-\mu x}}{\sqrt{x^2+\beta^2}}\,\mathrm{d}x = \frac{\beta\pi}{2}[H_1(\beta\mu)N_1(\beta\mu)] - \beta \equiv F(\mu,\beta), \tag{A.7}$$

where $H_1(\beta\mu)$ is the first order Struve function and $N_1(\beta\mu)$ is the first order Neumann function and the constraints for the constants $|arg\beta| < \frac{\pi}{2}$ and Re$\mu > 0$. By choosing $\beta = 1, \mu = t$ and integrating by parts we find that

$$F(\mu,\beta) = \left[e^{-tx}\sqrt{x^2+1}\right]_0^\infty + \int_0^\infty te^{-tx}\sqrt{x^2+1}\,\mathrm{d}x, \tag{A.8}$$

from which we can solve

$$\int_0^\infty te^{-tx}\sqrt{x^2+1}\,\mathrm{d}x = \frac{F(\mu,\beta)+1}{t}. \tag{A.9}$$

By substituting into eqn (A.6) we find that

$$\frac{EV(p_i)}{z_0}(x) = -t^2 \frac{\partial}{\partial t}\frac{F(\mu,\beta)+1}{t}. \tag{A.10}$$

The derivatives of the modified Bessel functions can be expressed as

$$\frac{\partial}{\partial x}N_1(x) = -N_2(x) + \frac{1}{x}N_1(x) \tag{A.11}$$

and

$$\frac{\partial}{\partial x}H_1(x) = \frac{1}{2}(H_0 - H_2 + \frac{x}{2\sqrt{\pi}\Gamma(\frac{5}{2})}), \tag{A.12}$$

with which we can express eqn (A.10) in the form

$$\frac{EV(p_i)}{z_0}(x) = \frac{\pi}{2}\left(H_1(t) - \frac{t}{2}\left(H_0 - H_2 + \frac{t}{2\sqrt{\pi}\Gamma(\frac{5}{2})}\right) - tN_2(t)\right). \tag{A.13}$$

Appendix B

CARDBOARD SAMPLES

Tab. B.1: The characteristics of cardboards and additives

Sample	grammage [g/m^2]	density [kg/m^3]	z-strength [kPa]
1	154.4	308	1.00
2	153.0	308	1.18
3	155.2	315	1.37
4	151.8	319	1.40
5	152.9	327	1.46
6	156.4	329	1.50
7	153.2	333	1.57
8	152.2	311	1.07

Appendix C

IMAGE PROCESSING

C.1 Surfaces determined by the carpet algorithm

Tab. C.1: The top and bottom surfaces and the thickness of samples as determined by the carpet program.

	Set 1			Set 2		
sample	top	bottom	d	top	bottom	d
1	71	291	221	53	270	218
2	61	259	199	66	268	203
3	51	258	208	51	254	204
4	57	258	202	64	265	202
5	72	262	191	60	249	190
6	62	253	192	55	258	202
7	68	255	188	53	243	191
8	57	268	212	72	269	198

C.2 Density calibration

Tab. C.2: The top and bottom surfaces and the thickness of samples as determined by the carpet program.

	Set 3			Set 4		
sample	top	bottom	d	top	bottom	d
1	51	242	192	52	241	190
2	57	232	176	56	235	180
3	59	230	172	55	233	179
4	61	231	171	71	243	173
5	72	238	167	66	225	160
6	66	232	167	67	234	168
7	65	235	171	69	238	170
8	57	244	188	71	251	181

Tab. C.3: Threshold gray scale values for sample set 1

sample	ρ_A [kg/m^2]	σ_{ρ_A}	Threshold value				
1	154.4	9.3	63	66	67	68	72
2	153.0	9.5	52	56	57	58	61
3	155.2	7.5	58	61	62	63	66
4	151.8	8.0	62	64	65	66	69
5	152.9	8.8	58	62	63	64	67
6	156.4	8.2	54	57	58	59	62
7	153.2	8.3	53	56	57	58	62
8	152.2	8.1	60	64	65	66	69

Tab. C.4: Threshold gray scale values for sample set 2

sample	ρ_A [kg/m^2]	σ_{ρ_A}	Threshold value				
1	154.4	7.7	54	55	56	57	59
2	153.0	7.3	49	51	52	53	55
3	155.2	6.9	53	54	55	56	58
4	151.8	7.6	56	58	59	60	62
5	152.9	6.6	52	54	55	56	57
6	156.4	7.4	54	56	57	58	60
7	153.2	7.3	54	56	57	58	60
8	152.2	6.9	49	51	52	53	55

Tab. C.5: Threshold gray scale values for sample set 3

sample	ρ_A [kg/m^2]	σ_{ρ_A}	Threshold value		
1	154.4	2.5	101	102	104
2	153.0	2.3	94	95	97
3	155.2	2.3	91	93	94
4	151.8	2.4	97	98	100
5	152.9	2.3	94	96	97
6	156.4	2.4	92	93	95
7	153.2	2.4	99	100	102
8	152.2	2.4	101	102	104

Tab. C.6: Threshold gray scale values for sample set 4

sample	ρ_A [kg/m^2]	σ_{ρ_A}	Threshold value		
1	154.4	2.3	120	122	123
2	153.0	2.3	119	121	122
3	155.2	2.3	115	117	119
4	151.8	2.3	115	116	118
5	152.9	2.3	109	111	112
6	156.4	2.3	117	119	121
7	153.2	2.3	120	121	123
8	152.2	2.5	113	115	117

Appendix D

RESULTS

D.1 Density profiles

Tab. D.1: Density profiles for sample set 1

sample	mean	std	slope	curvature
1	0.199	0.023	0.055	0.034
2	0.219	0.028	0.046	0.131
3	0.213	0.022	0.053	0.000
4	0.214	0.023	0.058	0.024
5	0.225	0.023	0.047	0.078
6	0.232	0.031	0.040	0.166
7	0.236	0.031	0.040	0.319
8	0.203	0.022	0.040	0.138

D.2 Contact densities

Tab. D.2: Density profiles for sample set 2

sample	mean	std	slope	curvature
1	0.206	0.025	0.043	0.190
2	0.216	0.029	0.034	0.252
3	0.220	0.020	0.053	0.047
4	0.215	0.025	0.053	0.124
5	0.228	0.029	0.043	0.263
6	0.222	0.023	0.059	0.093
7	0.230	0.034	0.050	0.367
8	0.219	0.027	0.043	0.276

Tab. D.3: Density profiles for sample set 3

sample	mean	std	slope	curvature
1	0.197	0.010	0.007	0.099
2	0.212	0.017	0.026	0.200
3	0.220	0.024	0.067	0.205
4	0.217	0.016	0.024	0.189
5	0.224	0.016	0.031	0.158
6	0.230	0.020	0.030	0.247
7	0.221	0.017	0.020	0.225
8	0.198	0.013	0.018	0.123

Tab. D.4: Density profiles for sample set 4

sample	mean	std	slope	curvature
1	0.198	0.013	0.006	0.161
2	0.208	0.015	0.029	0.175
3	0.212	0.014	0.027	0.131
4	0.212	0.018	0.049	0.141
5	0.232	0.018	0.043	0.166
6	0.227	0.016	0.038	0.121
7	0.221	0.016	0.016	0.201
8	0.204	0.018	0.056	0.091

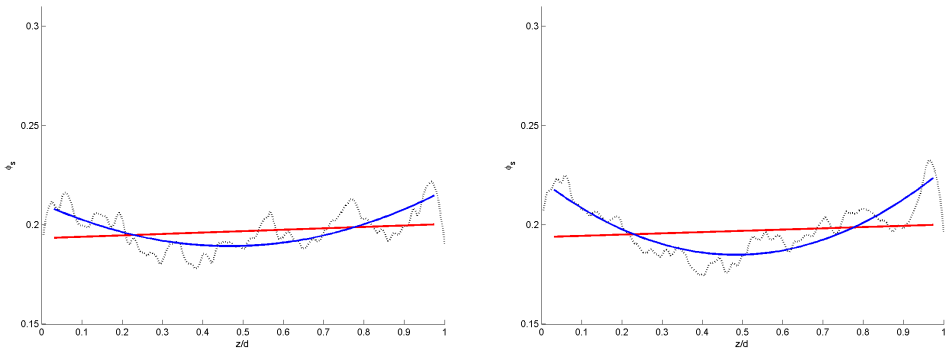

(a) Profile 13 (b) Profile 14

Fig. D.1: Profiles 1

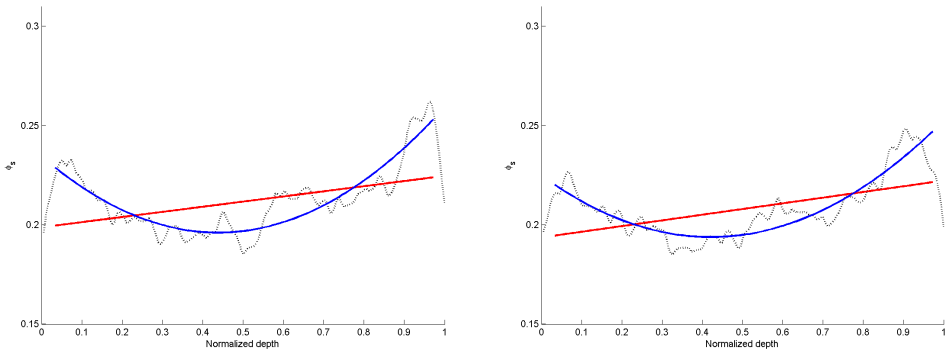

(a) Profile 23 (b) Profile 24

Fig. D.2: Profiles 2

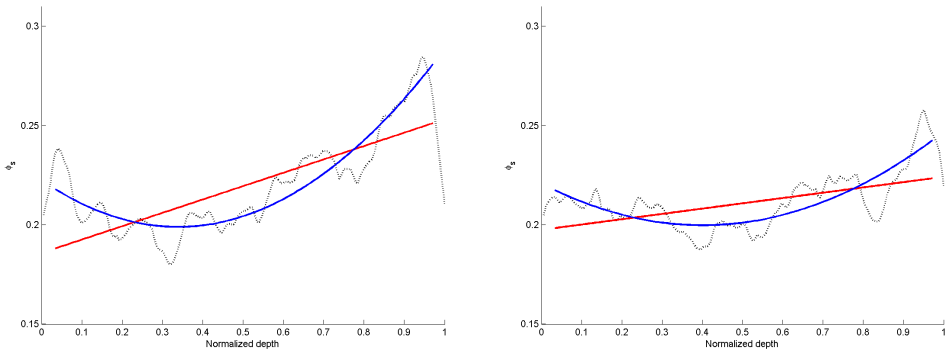

(a) Profile 33 (b) Profile 34

Fig. D.3: Profiles 3

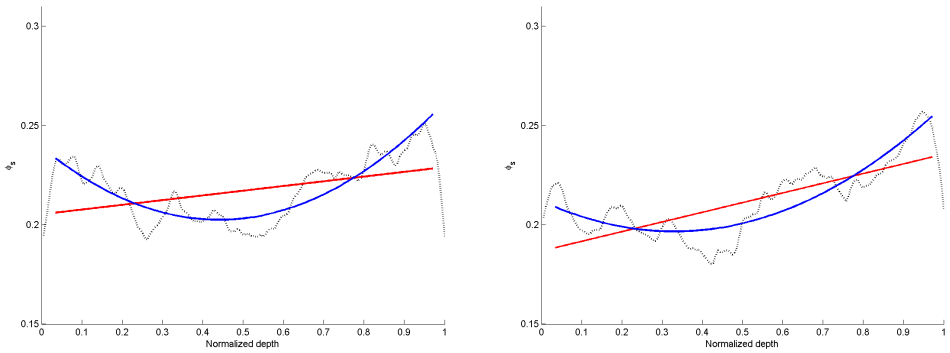

(a) Profile 43 (b) Profile 44

Fig. D.4: Profiles 4

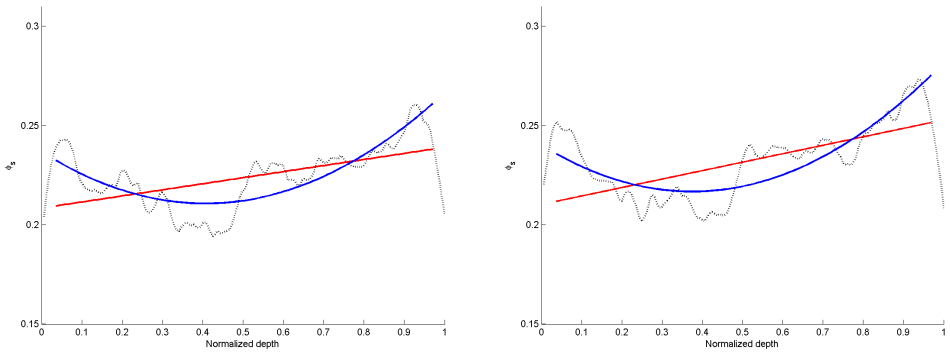

(a) Profile 53 (b) Profile 54

Fig. D.5: Profiles 5

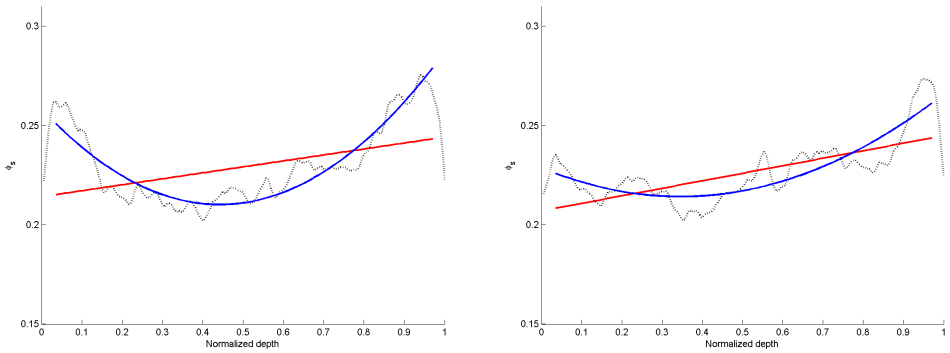

(a) Profile 63 (b) Profile 64

Fig. D.6: Profiles 6

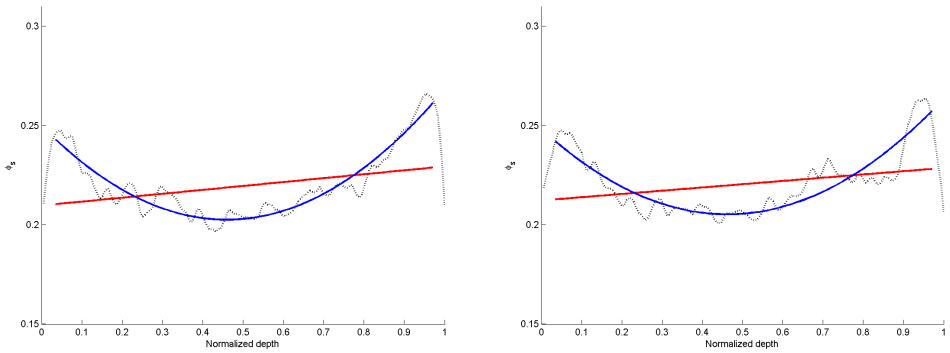

(a) Profile 73 (b) Profile 74

Fig. D.7: Profiles 7

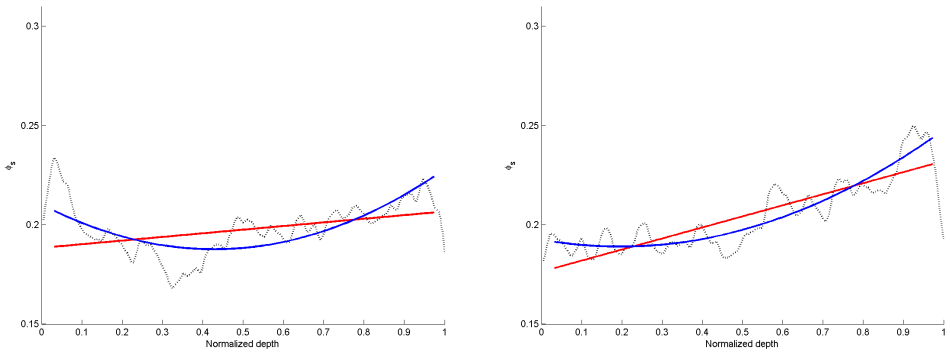

(a) Profile 83 (b) Profile 84

Fig. D.8: Profiles 8

Tab. D.5: The mean value and estimated error of parameter k

	Set 1		Set 2	
sample	<k>	δ_k	<k>	δ_k
1	0.229	0.002	0.215	0.0007
2	0.221	0.003	0.229	0.0011
3	0.217	0.004	0.2238	0.0001
4	0.218	0.004	0.219	0.001
5	0.2275	0.0004	0.225	0.001
6	0.228	0.002	0.232	0.003
7	0.2234	0.0005	0.235	0.001
8	0.2156	0.0005	0.229	0.001

Tab. D.6: The mean value and estimated error of parameter k

	Set 3		Set 4	
sample	<k>	δ_k	<k>	δ_k
1	0.2085	0.0005	0.2086	0.0001
2	0.2245	0.0004	0.2170	0.0004
3	0.2254	0.0003	0.2186	0.0002
4	0.2173	0.0006	0.2166	0.0002
5	0.2201	0.0001	0.2204	0.0004
6	0.2267	0.0008	0.2219	0.0002
7	0.2272	0.0004	0.2118	0.0005
8	0.2180	0.0001	0.2184	0.0006

Tab. D.7: The weighted mean and estimated error of solids contents ϕ_s and parameter k

sample	$<\phi_s>$	δ_{ϕ_s}	<k>	δ_k
1	0.198	0.003	0.2088	0.0001
2	0.211	0.003	0.2208	0.0003
3	0.216	0.003	0.2238	0.0001
4	0.215	0.003	0.2172	0.0001
5	0.224	0.003	0.2202	0.0001
6	0.228	0.003	0.2222	0.0002
7	0.222	0.003	0.2224	0.0003
8	0.202	0.003	0.2180	0.0001